



AMERICAN UNIVERSITY OF BEIRUT

DYNAMICS OF THIN ROTATING FLOWS SUBJECT TO  
ELECTRIC AND MAGNETIC FIELDS

by

AMANI IBRAHIM ZALZALI

A thesis  
submitted in partial fulfillment of the requirements  
for the degree of Master of Science  
to the Department of Physics  
of the Faculty of Arts and Sciences  
at the American University of Beirut

Beirut, Lebanon  
May 2014


AMERICAN UNIVERSITY OF BEIRUT

DYNAMICS OF THIN ROTATING FLOWS SUBJECT TO  
ELECTRIC AND MAGNETIC FIELDS

by

AMANI IBRAHIM ZALZALI

Approved by:



---

Dr. Ghassan Antar, Associate Professor  
Physics

Advisor



---

Dr. Issam Lakkis, Associate Professor  
Mechanical Engineering

Committee Member



---

Dr. Ghanem Oweis, Associate Professor  
Mechanical Engineering

Committee Member



---

Dr. Leonid Klushin, Professor  
Physics

Committee Member

Date of thesis defense: May 12<sup>th</sup>, 2014

AMERICAN UNIVERSITY OF BEIRUT


THESIS, DISSERTATION, PROJECT RELEASE FORM

Student Name: zalzali Amani Ibrahim  
Last First Middle

Master's Thesis       Master's Project       Doctoral Dissertation

I authorize the American University of Beirut to: (a) reproduce hard or electronic copies of my thesis, dissertation, or project; (b) include such copies in the archives and digital repositories of the University; and (c) make freely available such copies to third parties for research or educational purposes.

I authorize the American University of Beirut, **three years after the date of submitting my thesis, dissertation, or project**, to: (a) reproduce hard or electronic copies of it; (b) include such copies in the archives and digital repositories of the University; and (c) make freely available such copies to third parties for research or educational purposes.

      19/5/2014  
Signature      Date

This form is signed when submitting the thesis, dissertation, or project to the University Libraries



## ACKNOWLEDGEMENTS

First and foremost, I would like to express my sincere gratitude to my advisor, Dr. Ghassan Antar, for his continuous support during my study and research, for his patience, motivation, and enthusiasm. His guidance helped me in all the time of writing this thesis.

I would like to thank my committee members Dr. Issam Lakiss, Dr. Ghanem Oweis and Dr. Leonid Klushin. They generously gave their time to offer me valuable comments and questions.

I am grateful to my colleagues at the Laboratory for Plasma and Fluid Dynamics for sharing their expertise and scientific intuition especially during the weekly meetings: Moustafa Hammoud, Ali Asghar, Rodrique Bader, Dr. Daoud Baalbaki, Dr. Charbel Habchi and Ali Khalife. I appreciate their questions that helped me during my scientific and technical challenges. Special thanks go to my friends who supported me along the journey: Hanaa Aridi, Diala El Zein, Dr. Khairat Al Habbal, Ghina Halabi, Sehresh Abbasi, Zainab Balhas, Rouba Karam and Ali Badran. I greatly admire their friendship and I deeply appreciate their belief in me.

I would like to express my gratitude to my father, Ibrahim Zalzali, for his unconditional support and patience. I deeply thank my mother, Mona Chalhoub, for her love, caring and sacrifice. I am also thankful to my brother, Mohamad Zalzali, for his motivation and inspiration. Special thanks go to my fiancé Tarek Safwan for his love and encouragement.

# AN ABSTRACT OF THE THESIS OF

Amani Ibrahim Zalzali for Master of Science  
Major: Physics

Title: Dynamics of Thin Rotating Flows Subject to Electric and Magnetic Fields

We investigate the properties of thin rotating flows subject to a Lorentz force. The height of the fluid in motion is ten times smaller than its diameter allowing two-dimensional theory to be applied. This study is motivated by fundamental problems in nature related to geophysical flows, namely polar vortices and to accretion disks around black holes. In all of these areas, the main topic is the interplay between turbulence and average rotation. Using the Navier-Stokes equations with external Lorentz force, along with the appropriate boundary conditions, the base flow is found. Stability analysis using perturbation theory in slab geometry allows us to predict the unstable region of the flow. Experimentally, the fluid is a thin layer of Galinstan (liquid metal) placed in a cylindrical container. At its edge eight electrodes are biased with respect to a middle one in order to draw a current among them. A strong axial magnetic field is applied by permanent magnets. Using laser diagnostic technique, velocity fluctuations are measured versus several controlling parameters. It is shown that the fluid becomes unstable in absence of magnetic field fluctuations. This instability occurs in the  $(r, \theta)$ -plane and this is observed for the first time.

# CONTENTS

	Page
AKNOWLEDGEMENTS . . . . .	v
ABSTRACT . . . . .	vi
LIST OF ILLUSTRATIONS . . . . .	x
LIST OF TABLES . . . . .	xv
Chapter	
I. Introduction . . . . .	1
A. Motivation . . . . .	2
1. Accretion Disks . . . . .	2
2. Geophysical Fluid Dynamics . . . . .	4
3. Mechanical Engineering Applications . . . . .	6
B. Definitions . . . . .	7
C. Previous Work . . . . .	8
1. Unmagnetized Taylor-Couette Flows . . . . .	8
2. Magnetized Taylor-Couette Flows . . . . .	12
a. Balbus MRI . . . . .	13
b. Princeton MRI . . . . .	13
c. Helical Magnetorotational Instability (HMRI) . . . . .	15
3. Laboratory Quasi Two Dimensional Flows . . . . .	16
D. Thesis Plan . . . . .	19
II. Base Flow . . . . .	20

A. Introduction . . . . .	20
B. The Navier-Stokes Equations . . . . .	21
C. Base Flow of Taylor-Couette Flow (TCF) . . . . .	22
D. Base Flow of Thin Rotating Flow (TRF) . . . . .	26
E. Comparison Between TCF and TRF . . . . .	29
F. Conclusion . . . . .	31
<b>III. Stability Analysis . . . . .</b>	<b>32</b>
A. Introduction . . . . .	33
B. Axisymmetric Disturbances of Taylor-Couete Flow . . . . .	34
C. Non-Axisymmetric Distrurbances by Slab Approximation (TRF) . . . . .	37
1. Full Navier-Stokes Equations with Lorentz Force . . . . .	39
2. Form of Perturbation . . . . .	40
3. Steady State and Inviscid Limit . . . . .	40
4. Linearization . . . . .	41
5. Pressure Elimination and Coupling by Continuity . . . . .	41
6. Fourier Modes Analysis . . . . .	42
7. Stability Conditions . . . . .	43
D. Conclusion . . . . .	46
<b>IV. The Experiment and Laser Diagnostic . . . . .</b>	<b>48</b>
A. Introduction . . . . .	49
B. The Experimental Apparatus . . . . .	50
C. Fluid Characteristics . . . . .	51
D. External Magnetic Field . . . . .	53

E. Current Density . . . . .	55
F. Induced Magnetic Field . . . . .	57
G. Laser Diagnostics . . . . .	58
H. Fluid Distortions . . . . .	60
I. Shallow Water Equations . . . . .	60
J. Dimensionless Numbers . . . . .	64
K. Conclusion . . . . .	65
<b>V. Experimental Results . . . . .</b>	<b>66</b>
A. Introduction . . . . .	67
B. Experiment I: Motion as function of Electric Current . . . . .	68
C. Experiment II: Motion as function of Radial Position . . . . .	72
1. Steady State . . . . .	73
2. Unsteady State . . . . .	75
D. Conclusion . . . . .	78
<b>VI. Conclusion . . . . .</b>	<b>80</b>
A. Personal Achievements . . . . .	81
B. Future Work . . . . .	81
<b>Bibliography . . . . .</b>	<b>87</b>

# ILLUSTRATIONS

Figure	Page
<p>1. Left: Event horizon, accretion disk and gamma ray jets of a black hole (Source: Internet Encyclopedia of Science. Credit Astronomy: Roen Kelly). Right: Accretion disc and jet in a proto-star HH30 observed by the Hubble Space Telescope: the jet (in red) is perpendicular to the accretion disc. (Source: Burrows, STSci/ESA, WFPC2, NASA)) . . . . .</p>	3
<p>2. Left: A tornado approaching the town of Elie, Manitoba, Canada on June 22, 2007. It caused \$39 million in damage. Right: Hurricane Katrina which was the deadliest and most destructive Atlantic tropical cyclone of the 2005 Atlantic hurricane season. The total property damage was estimated at \$81 billion. . . . .</p>	5
<p>3. Schematic cutaway of the Rolls Royce Trent 1000 engine for the Boeing 787 Dreamliner, illustrating the bladed discs of the compressor and turbine. . . . .</p>	6
<p>4. Schematic drawings of the magnetized and unmagnetized Taylor Couette setups. A fluid is placed inside the gap between two concentric rotating cylinders with angular velocities <math>\Omega_1</math> and <math>\Omega_2</math>. The angular velocity of the fluid is <math>\Omega</math>. . . . .</p>	9
<p>5. Flow Regimes observed in Taylor-Couette apparatus in terms of inner and outer cylinder Reynolds numbers <math>R_i</math> and <math>R_o</math>. The dashed lines in the figure indicate the transition boundaries. Dotted lines indicate the expected, but not yet observed, continuation of several boundaries. . . . .</p>	10
<p>6. Left: The flow between concentric spheres with counter-rotating produces axisymmetric Taylor vortices. It is comparable to the vortices arising on the equator of the Earth. Near the poles, non-axisymmetric vortices arise. Right. Schematic drawing of Taylor-Couette setup showing counter rotating wavy vortices. . . . .</p>	12
<p>7. Experimental Setup of Princeton Experiment. . . . .</p>	14
<p>8. Sketch (left) and photograph (right) showing the central module of the PROMISE facility. . . . .</p>	16

9.	(a) Schematic representation of the experiment and (b) cross section of the experiment. . . . .	17
10.	Decaying Turbulence: Sequence of streak images of a laboratory experiment in a square tank. The fluid motion was initialized by towing a rake horizontally through the fluid from one side to the opposite side. The images are taken from 10 s until 55 min after towing the rake through the fluid. The initial state (at $t = 10$ s) is characterized by $L_0 \approx 0$ and $Re_* = 5000$ . The tails of the streaks are generated after digital processing of the images. . . . .	18
11.	In the laminar case, fluid particles travel in a straight line such that the velocity of the fluid remains constant in magnitude and direction. In the turbulent case, fluid particles start to swirl and move laterally leading to mixing in all directions such that the velocity becomes unpredictable. . . .	20
12.	Schematic drawing of Taylor-Couette apparatus. Two concentric cylinders with radii $R_1$ and $R_2$ rotate with angular velocity $\Omega_1$ and $\Omega_2$ . . . . .	23
13.	Schematic drawing of Thin Rotating Flow. A thin layer of a viscous and conducting fluid is situated in an axial magnetic field $\mathbf{B}$ and a radial current density $\mathbf{j}$ . The resulting Lorentz force, $\mathbf{f} = \mathbf{j} \times \mathbf{B}$ , in the azimuthal direction rotates the fluid. . . . .	26
14.	Velocity profiles versus normalized radius for several values of the electric current ( $\alpha = 150, 450, 750, 1000, 135$ ). As the current density increases, the maximum value of the velocity increases. . . . .	29
15.	Comparison of velocity profiles for TCF and TRF in arbitrary units. In the TC flow, $\Omega_1 = 4000s^{-1}$ and $\Omega_2 = 533/2s^{-1}$ according to one of the PRINCETON experiments. In TRF $\alpha = 3$ . . . . .	30
16.	(a) A perturbation to the system in a stable equilibrium results in the return to the stable position. (b) A perturbation in the unstable equilibrium results in the escape away from stable position. . . . .	33
17.	Sketch of Taylor-Couette Flow, An interchange of fluid between two rings means a change in angular momentum. . . . .	36
18.	Left. Axisymmetric Disturbances in the $(r, z)$ -plane. Right. Nonaxisymmetric Disturbances in the $(r, \theta)$ -plane. . . . .	38

19.	Slab Approximation. The $r$ -direction is becomes the $x$ coordinate, and the $\theta$ -direction becomes the $y$ coordinate. . . . .	39
20.	The methodology of analyzing the dispersion relation . . . . .	44
21.	Plot of $m^2$ versus $r/a$ for $n = 1, 2, \dots, 5$ for $I = 1$ A. . . . .	45
22.	Plot of $m^2$ versus $r/a$ for $I = 2, 4, 6,$ and $8$ A for $n = 2$ . . . . .	46
23.	Instabilities were studied in magnetized Taylor-Couette apparatus with axial magnetic field in Ref.[32, 36]. In the $\alpha\omega$ Dynamo experiment, the instability is also studied in the $(r, z)$ -plane using liquid sodium. In the Promise experiment, a helical magnetic field leads to the development of the instability. . . . .	50
24.	Experimental setup of rotating liquid metal. Eight outer electrodes are installed on the outer wall of a cylindrical container. A middle electrode is installed in the center of the container. The container is placed inside a set of two permanent magnets which generate an axial magnetic field. . .	51
25.	Rotating Galinstan in a cylindrical container under the effect of Lorentz force. . . . .	52
26.	Two ring magnets provide the external magnetic field. Measuring the external magnetic field using teslameter based on Hall Effect. . . . .	54
27.	Magnetic field measurements and a polynomial fit. . . . .	55
28.	Plot of magnetic field versus height for four different positions inside the inner diameter of the permanent magnets $r_0, r_1, r_2, r_3,$ and $r_4,$ where the distance between two consecutive positions is 5 cm. The magnetic field is measured backwards and forwards. . . . .	56
29.	Experimental setup for data collection. A: He-Ne Laser B: Mirror 1 C: Mirror 2 D: Rotating Mirror E: Permanent Magnets F: Electrodes G: Liquid Metal H: Power Supply I: Plexy Glass Cylinder J: Optical Table. . . .	58
30.	Schematic drawing showing the idea behind the experimental method. . .	59



31.	An incident beam of the laser falling on the surface is reflected by the fluid to point $P$ on the screen. When a passing wave deflects the surface by an angle $\alpha_{\perp}$ , the beam is reflected to point $S$ on the screen. When a passing wave deflects the surface by an angle $\alpha_{\parallel}$ , the beam is reflected to point $Q$ on the screen. . . . .	61
32.	Experimental method to find the azimuthal velocity. . . . .	62
33.	Laser shining on the surface of the fluid showing the surface deflection perpendicular to the plane of the laser beam. . . . .	63
34.	Laser shining on the surface of the fluid showing the surface deflection parallel to the plane of the laser beam. . . . .	63
35.	Distortion of the fluid surface caused by the rotation of the flow leads to large scale motion. Perturbation of the distorted surface due to instabilities leads to small scale motion. . . . .	67
36.	In the first experiment, measurements at four different positions of the fluid surface are collected. At each position, measurements of eleven values of the current are taken. . . . .	68
37.	The laser reflection on the screen is analyzed by MATLAB as the point of highest intensity. A filter is applied to sharpen the image. . . . .	69
38.	Plot of laser reflections as function of current showing an increase of the distances between them as an indication of growing instability. . . . .	71
39.	Plot of standard deviations versus current at four different positions of the fluid. . . . .	72
40.	In the second experiment, the laser beam probes the surface of the fluid. This measurement is collected for eight different values of the current. . .	73
41.	Trajectory of laser reflection for several currents between 1 and 7 A. . . .	74
42.	An average trajectory along with error bars of the same measurement of probing the surface at fixed current repeated 5 times. . . . .	77

43. Up: The average  $Y$  component (red line) along with the  $Y$  components of the five measurements (blue). Down: Standard deviation of the  $Y$  component (blue) and smoothing of the curve(red). . . . . 77

44. Plot of the standard deviation of the  $y$ -component of the position of the laser reflection versus radius. . . . . 78

# TABLES

Table		Page
1.	Comparison between TCF and TRF . . . . .	30
2.	Setup Dimensions . . . . .	52
3.	Properties of Galinstan and Water . . . . .	53
4.	Dimensionless Numbers TRF . . . . .	64

CHAPTER I  
INTRODUCTION

## **A. Motivation**

Understanding the fundamental physics behind rotating flows is important for early predictions in geophysical fluid dynamics and understanding the mysteries of the universe in astrophysics. Cyclones in the atmosphere, circulations in the ocean, and accretion disks in the universe are all essentially rotating flows.

The dynamics of rotating flows are studied in a thin layer of liquid metal that is subject to a radial electric current and axial external magnetic field. The resulting Lorentz force caused by the electric and magnetic fields rotates the fluid. The thickness of the fluid layer is kept small to ensure the applicability of two dimensional theory. We treat this problem analytically by introducing external forcing to Navier Stokes equations. An experiment is conducted in order to study the characteristics of the flow as well as the onset of two dimensional non-axisymmetric centrifugal instability (2D-NACI).

This study has wide applications in naturally occurring rotating flows such as astrophysical and geophysical fluid dynamics. It also contributes to the development of mechanical designs of hydrodynamical systems. In the next section, we present the fields of application.

### ***1. Accretion Disks***

An accretion disk is a flow of gas, plasma, dust or particles around any astronomical object. This object can be a white dwarf, a neutron star, or a black hole in which the material orbiting in the gravitational field of the object loses energy and angular momentum due to turbulence and viscosity. This dissipation of energy causes the orbits of the disk to acquire a spiral nature as shown in Fig.(1)). Experiments that simulate the fluid motion in an accretion disk in a laboratory help astrophysicists bring theoretical models of accretion disks closer to reality.

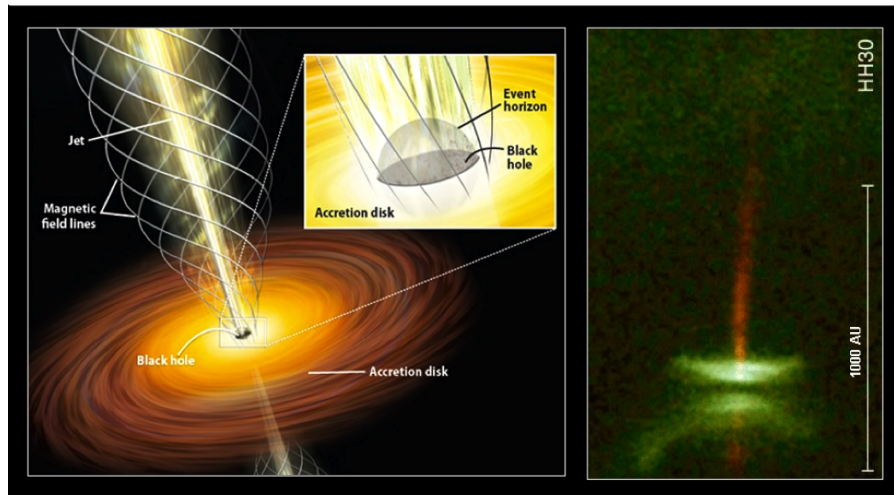


Figure 1: Left: Event horizon, accretion disk and gamma ray jets of a black hole (Source: Internet Encyclopedia of Science. Credit Astronomy: Roen Kelly). Right: Accretion disc and jet in a proto-star HH30 observed by the Hubble Space Telescope: the jet (in red) is perpendicular to the accretion disc. (Source: Burrows, STSci/ESA, WFPC2, NASA))

The formation of an accretion disk starts when matter possesses enough angular momentum such that it cannot simply fall towards the central accretor in a straight line. Because rotation resists the inflow of matter, the flow flattens in the direction perpendicular to the rotation axis therefore giving it a disk shape structure. In the direction parallel to the rotator axis, thermal pressure and gravitaional force balance each other. This contracts the disk and reduces its thickness to become thin. This geometry allows us to consider the flow of particles in an accretion disk quasi-two dimensional.

It was observed that the rates of accretion in these disks are so high that the molecular viscosity of astrophysical gases and plasma is not insufficient to explain the high rates. The need to conduct laboratory experiment is then necessary. Several studies were inspired by the Taylor-Couette experiments, to be introduced in this chapter, to study the possible instabilities arising in accretion disks. However, the exact type of instability leading to the high accretion rates is still debatable.

In this thesis, we study the hydrodynamic instability arising in a fluid of similar geometry a thin accretion disk, which helps us understand the dynamics of the accretion disk flow. Of greater importance, the study of linear growth phase and saturation of the instability provides much needed insight and useful benchmarks against which to compare simulations of accretion disks around black holes.

## ***2. Geophysical Fluid Dynamics***

Without its atmosphere and oceans, our planet would not sustain life. The natural fluid motion occurring in these systems is then of vital importance and their study is essential. Laboratory experiments, such as the one conducted in this research work, are considered as idealized environments of complicated dynamics of geophysical structures. Thanks to advances in geophysical fluid dynamics, the ability to predict the path of tornadoes and hurricanes has improved tremendously over the past decades. Fig. (2) shows Hurricane Katrina which was the costliest natural disaster, as well as one of the five deadliest hurricanes, in the history of the United States taking over 1600 lives [1]. Fig.(2) also shows Elie, the strongest confirmed tornado in Canadian history [2].



Figure 2: Left: A tornado approaching the town of Elie, Manitoba, Canada on June 22, 2007. It caused \$39 million in damage. Right: Hurricane Katrina which was the deadliest and most destructive Atlantic tropical cyclone of the 2005 Atlantic hurricane season. The total property damage was estimated at \$81 billion.

The motion observed in both the oceans and the atmosphere exhibit a wide range of scales and depend on an interplay of many parameters. In order to avoid an excessive degree of complexity, most laboratory experiments isolate a single process in order to study in detail. Therefore, the design of independent experiments then strongly contributes to the overall picture of understanding geophysical flows.

Although it is difficult to set an exact thickness to the atmosphere of the Earth (due to the lack of definite boundary layer) 30 km above the Earth surface encompass 99% of its atmospheric mass. The radius of the Earth is around 6400 km, so the atmosphere is less than 1% of the Earth radius. Therefore, the dynamics occurring in the atmosphere, like horizontal rotations of tornadoes and hurricanes are considered to be quasi two dimensional flows. Similarly, the oceans thickness is less than 10 km thus allowing circulations parallel to the surface to become far larger than the rotations in the perpendicular plane, which are suppressed. This thesis studies instabilities in two di-



mensional rotating flows. Hence, the instabilities developing in the experiment conducted in this thesis are similar to those occurring in the oceans and atmosphere.

Shallow Water Equations (SWE), adopted from geophysical fluid dynamics, provide us with a method in the diagnostics chapter to extract properties of the fluctuations of the velocity of the fluid.

### ***3. Mechanical Engineering Applications***

Rotating flows are also encountered in engineering designs. For higher efficiency of mechanical systems with rotating fluids, the understanding of rotating flows is highly beneficial. For example, in a gas turbine engine such as the one shown in Fig.(3), stationary discs in cylindrical geometries are surrounded by empty cavities filled with air.

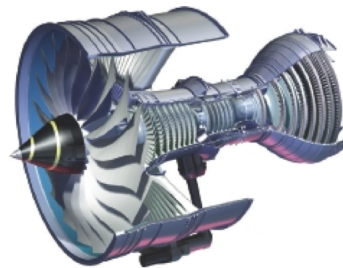


Figure 3: Schematic cutaway of the Rolls Royce Trent 1000 engine for the Boeing 787 Dreamliner, illustrating the bladed discs of the compressor and turbine.

The cavity formed contains a rotating disc adjacent to a stationary disc (wheelspace or rotor-stator disc cavity to mechanical engineers). Cooling this air reduces the thermal load on the disc and prevents the entry of hot mainstream gas from the blade path into the cavity. However, the use of this air is harmful to engine cyclic performance. Tur-

bine efficiency can be also adversely affected by the seal air efflux into the main annulus. The lifetime of the rotor, and the cyclic and component performance of the engine are therefore dependent on the efficiency with which the cavity is purged of hot gases[3].

To determine the power required to overcome frictional drag, local flow characteristics, and associated heat transfer, scientists and engineers were motivated to investigate a number of rotor-stator disc configurations. Therefore, the study of rotating flows in laboratory experiments contributes to optimizing the best design with the most convenient parameters.

## B. Definitions

In order to generalize different experimental results in fluid mechanics, dimensionless parameters are introduced:

- Reynolds number ( $Re$ ) is a dimensionless number that gives a measure of the ratio of inertial forces to viscous forces and consequently quantifies the relative importance of these two types of forces for a given flow. The higher the Reynolds number is, the more turbulent the flow is:

$$Re \sim \frac{\mathbf{u} \cdot (\nabla \mathbf{u})}{\mu \nabla^2 \mathbf{u}} \sim \frac{uL}{\nu} \quad (1)$$

where  $L$  is the characteristic length of the fluid container,  $u$  is the velocity of the fluid and  $\nu$  is the kinematic viscosity of the fluid.

- Hartman number ( $Ha$ ) is dimensionless number that gives the ratio of the electromagnetic force to the viscous force.

$$Ha^2 \sim \frac{\mathbf{j} \times \mathbf{B}}{\mu \nabla^2 \mathbf{u}} \sim \frac{\sigma \Delta VB}{\mu u} + \frac{\sigma B^2 L^2}{\mu} \quad (2)$$

where  $B$  is the magnetic field,  $\sigma$  is the electric conductivity.

- Prandtl number ( $Pr$ ) is a dimensionless parameter of the ratio of conduction to . It can be used to determine which process will win. If a fluid is more viscous, the Prandtl number is greater and the heat transfer will be less convective.

$$Pr = \frac{\nu}{\kappa} \quad (3)$$

where  $\kappa$  is the thermal diffusivity.

- Ekman number ( $E_k$ ) is a dimensionless number used in describing geophysical phenomena in the oceans and atmosphere. It characterizes the ratio of viscous forces in a fluid to the fictitious forces arising from planetary rotation.

$$E_k = \frac{\nu}{\Omega L^2} \quad (4)$$

## C. Previous Work

Experiments which aim at studying rotating flow belong to several areas of research. In this section, we distinguish three main areas: Unmagnetized Taylor-Couette flows, Magnetized Taylor-Couette flows, and laboratory quasi two dimensional flows.

### 1. *Unmagnetized Taylor-Couette Flows*

Mallock and Couette both independently developed a method to accurately measure the viscosity of several fluids using two differentially rotating concentric cylinders

[4, 5], now known as a Taylor-Couette flow.

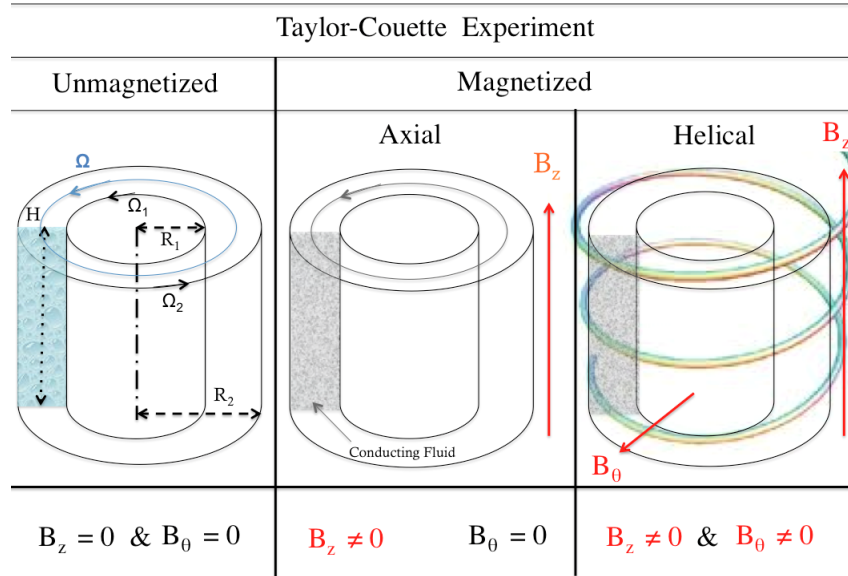


Figure 4: Schematic drawings of the magnetized and unmagnetized Taylor Couette setups. A fluid is placed inside the gap between two concentric rotating cylinders with angular velocities  $\Omega_1$  and  $\Omega_2$ . The angular velocity of the fluid is  $\Omega$ .

A circular Couette system, shown in Fig.(4), is characterized by the several control parameters: the radius ratio  $\eta = R_1/R_2$ , where  $R_1$  and  $R_2$  are the inner- and outer-cylinder radii; the aspect ratio  $\Gamma = H/(R_2 - R_1)$ , where  $H$  is the height of the fluid; the inner- and outer-cylinder Reynolds numbers  $Re_{1,2} = R_1(R_2 - R_1)\Omega_{1,2}/\nu$  where  $\nu$  is the kinematic viscosity of the fluid,  $\Omega_1$  and  $\Omega_2$  are the angular velocities of the inner and the outer cylinders respectively.

When Mallock rotated the inner cylinder keeping the outer cylinder fixed in his experiment, vortices developed in the flow bringing the attention of instability to Lord Rayleigh in 1895. While Rayleigh's analysis in 1916 explained the physical origin of the vortical structure [6], it was not until 1923, that G. I. Taylor was able to relate the

theory to the experiment for stability in cylindrical Couette flow. His investigation was a key development in the modern study of fluid dynamics. It offered convincing proof that the Navier-Stokes equations indeed accurately describe the flow of a Newtonian fluid, not just at the base flow level, but also for the analysis of secondary flows and instabilities. Furthermore, it was the first successful application of linear stability analysis that accurately predicted experimental results, namely the transition from stable flow to vortical Taylor-Couette flow [7].

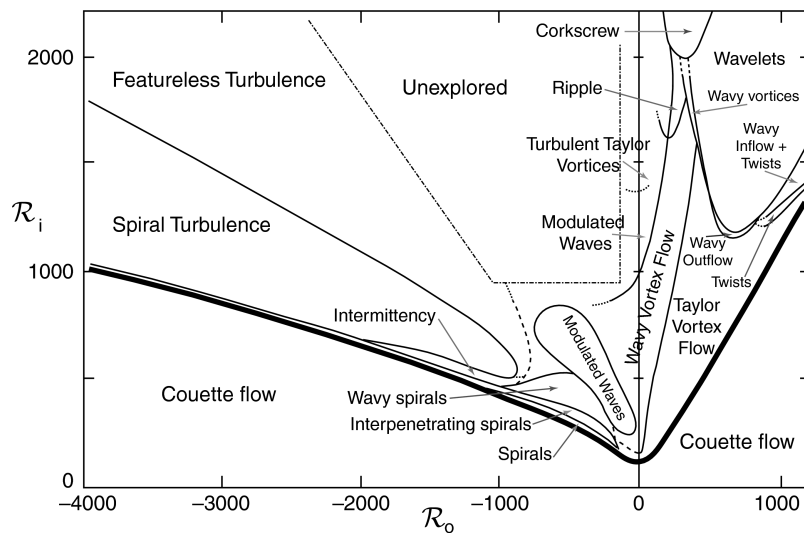


Figure 5: Flow Regimes observed in Taylor-Couette apparatus in terms of inner and outer cylinder Reynolds numbers  $R_i$  and  $R_o$ . The dashed lines in the figure indicate the transition boundaries. Dotted lines indicate the expected, but not yet observed, continuation of several boundaries.

Many scientists continue to investigate the motion in a Taylor-Couette setup. In 1965, Coles realized that the azimuthal flow between counter-rotating cylinders was unstable to non-axisymmetric spiral vortices. In his remarkable study of flows between both counter- and co-rotating cylinders, Coles discovered several distinctive flows including

intermittent turbulent bursts and spiral turbulence [8]. In 1968, Snyder compared his observations of the most unstable wavenumber of spiral vortices between counter-rotating cylinders with the predictions of Krueger, Gross & DiPrima [9, 10, 11]. In 1970, Snyder found that for  $\eta = R_1/R_2 = 0.2, 0.5, 0.8$  and 0.959 a variety of waveforms occur for small  $Re$  in both counter- and co-rotating cylinders [12]. In 1983, Andereck et al. reported the observation of five new flows occurring between co-rotating cylinders [13]. The understanding of flow regimes in terms of the Reynolds numbers of the inner and outer cylinders has developed over the years to enclose most of the possible combinations of inner and outer Reynolds numbers. These achievements are summarized in Fig.(5).

Most of the studies of Taylor-Couette system of fluid motion is done in narrow gap limit, or in other words large aspect ratios. In this limit, the vertical boundaries (or end-caps) between the cylinders do not have a dynamical role, even with finite viscosity [14].

Studies of Taylor-Couette flows can be applied to geophysical flows with axial symmetry such as the rotations arising near the equator of the Earth as shown in 6. Towards the poles, polar vortices develop giving rise to non-axisymmetric instabilities. In this thesis, we study two dimensional non-axisymmetric centrifugal instabilities in a thin rotating layer of fluid.

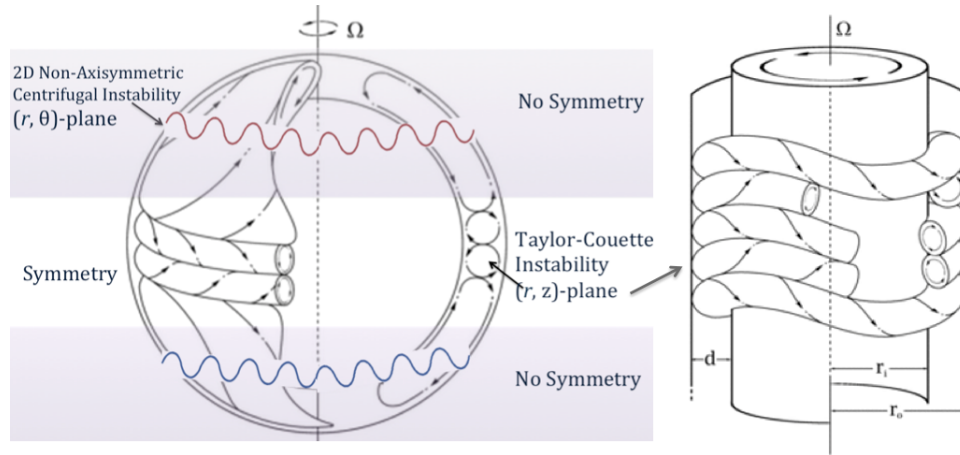


Figure 6: Left: The flow between concentric spheres with counter-rotating produces axisymmetric Taylor vortices. It is comparable to the vortices arising on the equator of the Earth. Near the poles, non-axisymmetric vortices arise. Right. Schematic drawing of Taylor-Couette setup showing counter rotating wavy vortices.

## 2. Magnetized Taylor-Couette Flows

Taylor-Couette flows are commonly used to study instabilities leading to turbulence. In presence of an external magnetic field, the fluid becomes magnetized and the growth rates of instabilities are affected. In this thesis, we distinguish between two types of instabilities: Magnetorotational Instability (MRI) and Rayleigh centrifugal instability.

Magnetorotational instability (MRI) was discovered by Velikhov in 1959 in the context of vertically magnetized Taylor-Couette flow. His analysis was generalized by Chandrasekhar in 1960 using a variational principle. Gases or liquids containing mobile electrical charges are subject to the influence of a magnetic field. In addition to hydrodynamical forces such as pressure and gravity, an element of magnetized fluid also feels the Lorentz force  $J \times B$ , where  $J$  is the current density and  $B$  is the magnetic field vector. If the fluid is in a state of differential rotation about a fixed origin, this Lorentz force can be surprisingly disruptive, even if the magnetic field is very weak. This process is known as

the Magnetorotational Instability, or MRI. [15]

Centrifugal instability is due to the imbalance between the radial pressure gradient and the centrifugal force in a rotating fluid. In 1917, Rayleigh stated a necessary condition for the existence of a centrifugal instability:

$$\frac{\partial(r^2\Omega)^2}{\partial r} < 0$$

where  $\Omega$  is the angular velocity.

Assuming that  $\Omega \sim r^\delta$ , stability analysis of the distribution of angular velocity leads to the conclusion that for  $\delta > -2$  Couette-like hydrodynamic flows are unstable.

a. Balbus MRI

Balbus and Hawley published a pioneering work in 1991 showing that a broad class of astrophysical accretion disks is dynamically unstable to axisymmetric disturbances in the presence of a weak magnetic field [16]. Axisymmetric large wavenumber Eulerian perturbations with space-time dependence  $\exp(i(k_r r + k_z z + \omega t))$ , with a vertical magnetic field  $B_z(r, z)\hat{\mathbf{z}}$  and an azimuthal magnetic field  $B_\Phi(r, z)\hat{\boldsymbol{\phi}}$  have led to show the existence of very powerful shearing instability imposed by a weak magnetic field, which they called the magnetorotational instability. The fluctuations in the magnetic field  $(\delta B_r, \delta B_\Phi, \delta B_z)$  are necessary ingredients in the stability analysis to derive the criterion showing the destabilizing effect of the magnetic field.

b. Princeton MRI

The theoretical explanation provided by Balbus and Hawley has inspired several experiments to use rotating liquid metals in magnetized Taylor-Couette setups to



induce MRI in the laboratory. The group at Princeton University has been active in this field, highly contributing to the progress of the topic through experimental and numerical achievements. The setup is shown in Fig.(7).

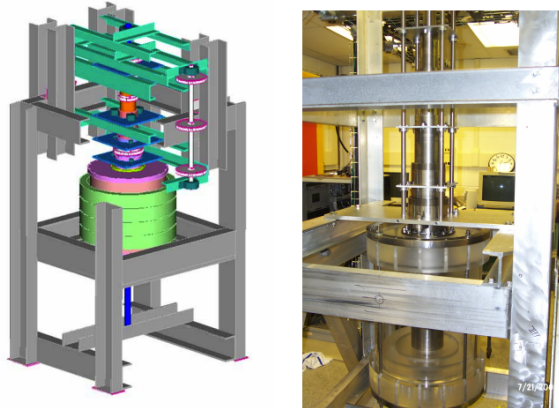


Figure 7: Experimental Setup of Princeton Experiment.

A challenge for the Princeton experiment was to set up an initial rotation profile that is stable to the Taylor-Couette instability (TCI) while unstable to the magnetorotational instability (MRI) when an appropriate magnetic field is applied. The results were compared to simulations and it was found that after turning vertically along the inner cylinder, these flows converge at the midplane and depart the boundary in a radial jet [17]. The authors investigated the reason and attributed this phenomena to Ekamn circulation.

In Ref.[18], local WKB methods to survey the MRI regime for realistic materials and laboratory parameters showed that the most unstable modes have wavelengths twice as large as the apparatus, so that WKB methods are not to be trusted apriori. In their second paper, the authors apply global linear analysis. They integrate the full set of viscous

and resistive equations via an initial-value scheme to obtain numerical growth rates for cases that would be stable by Rayleigh's criterion.

c. Helical Magnetorotational Instability (HMRI)

It was shown by Hollerbach et al. that the threshold for the onset of the magnetorotational instability in a Taylor-Couette flows can be dramatically reduced if an azimuthal magnetic fields is imposed on the flow. In agreement with this prediction, Stefani et al. presented results of their Taylor-Couette experiment with the liquid metal alloy (GaInSn), showing evidence for the existence of the magnetorotational instability at Reynolds numbers of the order of 1000 and Hartmann numbers of the order of 10. Promise facility, the Taylor-Couette setup, is a cylindrical vessel made of copper which is filled with a liquid metal called Galinstan (Fig. 8). Liu et al. presented a WKB analysis of the helical magnetorotational instability HMRI, and claimed that it does not exist for Keplerian rotation profiles [19]. Later, Hollerbach et al. showed that if radial boundary conditions are included, the HMRI can exist even for rotation profiles as flat as Keplerian, provided only that at least one of the boundaries is sufficiently conducting [20].

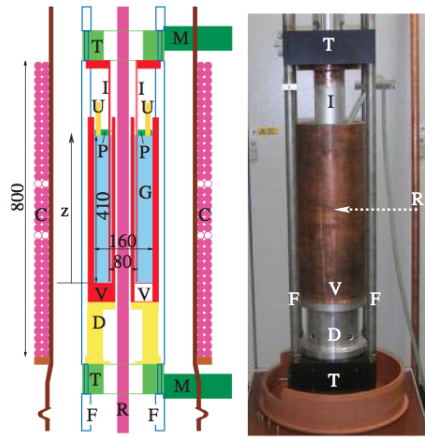


Figure 8: Sketch (left) and photograph (right) showing the central module of the PROMISE facility.

### 3. *Laboratory Quasi Two Dimensional Flows*

Two dimensional turbulence phenomena can be observed in the atmosphere and oceans, such as the inverse energy cascade and zonal flows, which can be reproduced and studied in simple laboratory experiments [21]. These experiments provide a valuable tool to develop models to simulate critical properties of the atmospheric and oceanic activities for a better prediction of the climate [22].

To study quasi two dimensional turbulence, several authors [21, 23, 24, 25, 26] have carried out experiments in an electromagnetically forced thin fluid layer in a square Plexiglass container. A schematic drawing of the setup is shown in Fig.(9). The container is filled with a conducting fluid. At the sidewalls, electrodes are placed and connected to a current supply. Below the fluid, a set of permanent magnets are placed in a geometry depending on the vortex structures desired to be produced by the Lorentz force  $F = j \times B$ .

Van Heijst et al. studied the effects of solid boundaries on confined two dimensional decaying turbulence. The experiments were carried out in a square container of

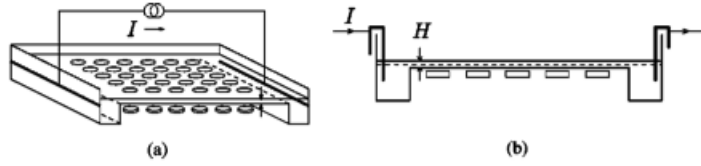


Figure 9: (a) Schematic representation of the experiment and (b) cross section of the experiment.

dimensions  $(100 \times 100 \times 30) \text{ cm}^3$  which was filled with a two-layer salt stratification, consisting of a layer of fresh water on top of a layer of salty water, separated by an interfacial layer of typically a few centimetres depth [27]. A typical sequence of streak images taken during an experiment with approximately zero initial angular momentum ( $L_0 \approx 0$ ) is shown in Fig.(10). In the early stage of the flow evolution, the small-scale motions introduced by the moving grid are clearly visible. It also shows how the flow becomes gradually dominated by larger vortex structures. At a later stage (at  $t = 55$  min) the flow consists of one large circulation cell and a small cell of opposite circulation. This double-cell structure was rather persistent, and continued to revolve until in the very late final state it has changed into one single cell filling the domain completely [27].

In Ref.[24], forced shear flows in a thin layer of an incompressible viscous fluid were studied. Photographs were used to obtain the stream function of vortical flow patterns arising after the primary shear flow loses stability. Various flow characteristics are determined and results are compared to the stability theory of quasi-two-dimensional flows. The applicability of the quasi-two-dimensional approximation is directly verified and the possibility of reconstruction of the driving force from the secondary flow pattern is demonstrated.

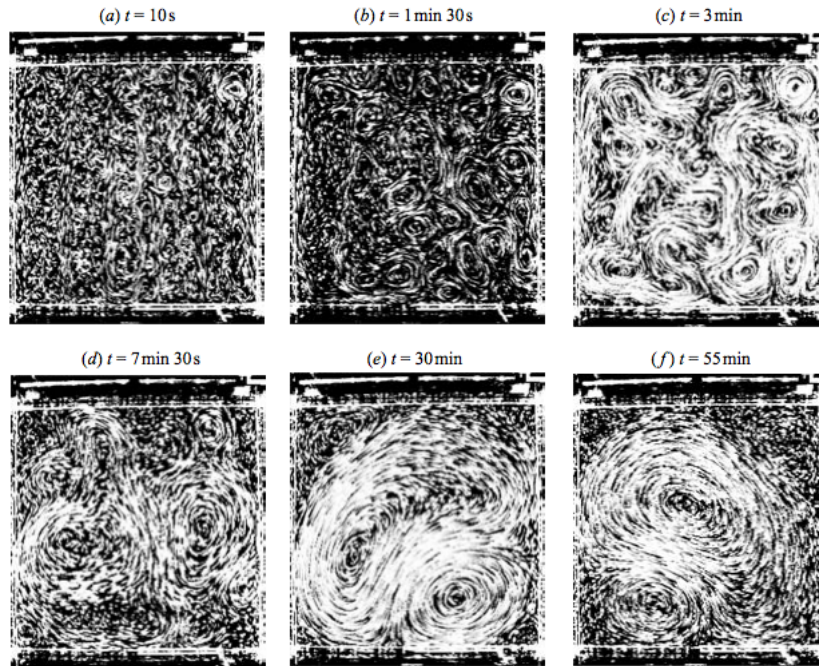


Figure 10: Decaying Turbulence: Sequence of streak images of a laboratory experiment in a square tank. The fluid motion was initialized by towing a rake horizontally through the fluid from one side to the opposite side. The images are taken from 10 s until 55 min after towing the rake through the fluid. The initial state (at  $t = 10$  s) is characterized by  $L_0 \approx 0$  and  $Re_* = 5000$ . The tails of the streaks are generated after digital processing of the images.

One of the main features of the dynamics of the viscous global geophysical flows is that the dissipation of their kinetic energy is mainly due to friction of free atmosphere over so called geophysical boundary layers (GBL). In Ref. [25], the role of bottom friction in shallow fluid layers is studied in the experimental setup as described above. In particular, the power-law behavior of the kinetic energy and the bottom-drag coefficient are investigated. For further details, two excellent review articles are by Tabeling (2002) [28] and a more recent one by Clercx and van Heijst (2009)[29].

## **D. Thesis Plan**

In the next chapter, the base flow of a fluid in a Taylor-Couette setup is derived. Also, the base flow of a thin layer of conducting fluid subject to electric and magnetic fields is derived using Navier–Stokes equations in a cylindrical symmetry with an external Lorentz force.

Chapter III includes the stability analysis of the thin rotating flow. Perturbation theory leads to the determination of the onset of instability of the flow versus several parameters.

Chapter IV describes the experimental apparatus as well as the experimental methods which we have developed to extract wave properties of the fluid. Using laser diagnostics, we study the dynamics of the flow.

Chapter V displays the experimental results which we have collected using the methods described in the chapter IV. Several experiments were performed to determine the onset of the instability. It also presents the results of image processing and data analysis.

Chapter VI includes a summary of the thesis, final remarks on the experimental methods and a vision of future work.

# CHAPTER II

## BASE FLOW

### A. Introduction

In fluid mechanics, a flow may experience a transition from a laminar to turbulent regime. A laminar flow is the time-reversible behavior of particles traveling smoothly in streamlines. Flow properties such as velocity and pressure remain constant as function of time. A turbulent flow is the time-dependent chaotic behavior of particles. In a turbulent flow, the velocity at a given point varies unpredictably in magnitude and direction. In Fig.(11), an example of laminar versus turbulent flow is shown.

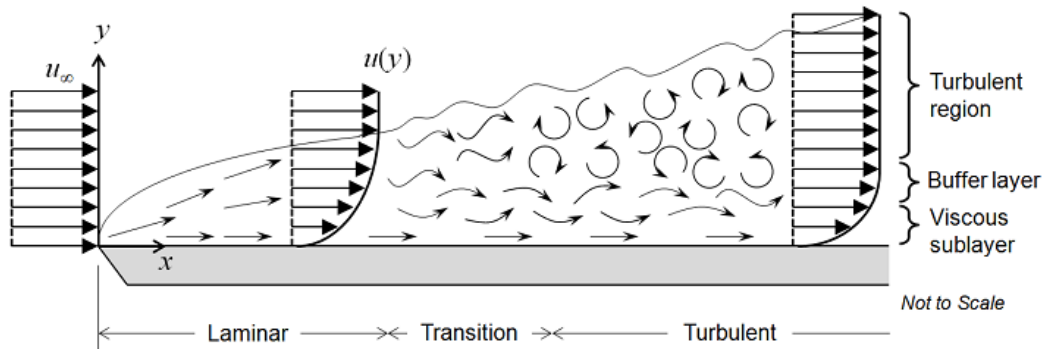


Figure 11: In the laminar case, fluid particles travel in a straight line such that the velocity of the fluid remains constant in magnitude and direction. In the turbulent case, fluid particles start to swirl and move laterally leading to mixing in all directions such that the velocity becomes unpredictable.

In this chapter, we study the laminar flow of a thin rotating layer of conducting liquid metal subject to electric and magnetic fields. As we have seen in the introduction, this study is closely related to the study of liquids situated between two rotating cylinders. Thus, we derive the expression of the azimuthal velocity in the laminar case of a

fluid rotating between two concentric cylinders (Taylor-Couette Flow) and then apply the same steps to obtain the azimuthal velocity of a thin rotating flow (TRF). The velocity is expressed in terms of geometrical and experimental parameters such as the size of the container, height of the fluid, magnitude of the magnetic field, current density and fluid viscosity. Finally, the velocities of both flows are compared.

## B. The Navier-Stokes Equations

The equations governing the motion of fluids are called the Navier-Stokes equations:

$$\rho \left( \underbrace{\frac{\partial \mathbf{u}}{\partial t}}_{\text{Acceleration}} + \underbrace{\mathbf{u} \cdot \nabla \mathbf{u}}_{\text{Convective Term}} \right) = \underbrace{-\nabla p}_{\text{Pressure Gradient}} + \underbrace{\mu \nabla^2 \mathbf{u}}_{\text{Viscosity}} + \underbrace{\mathbf{f}}_{\text{External Forces}} \quad (5)$$

The continuity equation is:

$$\frac{\partial \rho}{\partial t} + \rho(\nabla \cdot \mathbf{u}) = 0 \quad (6)$$

where  $\rho$  is the density of the fluid,  $\mathbf{u}$  is the velocity,  $p$  is the pressure,  $\mu$  is the dynamic viscosity of the fluid and  $\mathbf{f}$  is the sum of all external forces.

Inertia is the property of an object to remain at a constant velocity, unless an outside force acts on it. The above equation is a balance between the inertia terms on one side and the divergence of stress along with the external body forces on the another side. An object with a large inertia will resist strongly to a change in velocity. However, an object with a small inertia will almost instantaneously move when acted upon by a force. The inertia of fluid flows is caused by non-linear interactions within the flow field. These non-linearities may cause instabilities in the flow to grow, and therefore the flow can get turbulent when inertial effects are dominant.

The terms in the Navier-Stokes equations can be explained as follows:



- $\partial \mathbf{u} / \partial t$  represents the acceleration. When this equation is equal to zero, it means that the velocity at a given point is not changing over time.
- $(\mathbf{u} \cdot \nabla \mathbf{u})$  represents the convective term of the flow field. It is the non linear effect of the acceleration of a fluid with respect to space.
- $\nabla p$  is the spatial gradient of pressure. It is the effect of stresses such as pressure and shear stress in the fluid.
- $\mathbf{f}$  represents the vector field of the sum of all external forces, such as gravitational or electromagnetic forces.
- $(\mu \nabla^2 \mathbf{u})$  is an internal force, which is due to the fact that in a flowing fluid, there can be a shearing stress. This is called the viscous force.

The continuity equation in fluid dynamics states that in any steady state process, the rate at which mass enters a system is equal to the rate at which mass leaves the system. If  $\rho$  is a constant, as in the case of incompressible flow, the mass continuity equation simplifies to  $\nabla \cdot \mathbf{u} = 0$ .

### C. Base Flow of Taylor-Couette Flow (TCF)

In this section, we derive the expression of azimuthal velocity of TCF. Taylor-Couette flow corresponds to the motion of viscous fluid confined between two rotating cylinders as shown in Fig.(12). Neglecting gravity, the remaining forcing terms acting on the fluid are the gradient of pressure and viscosity.

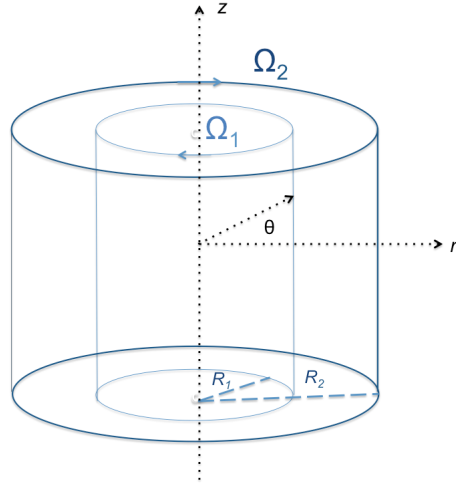


Figure 12: Schematic drawing of Taylor-Couette apparatus. Two concentric cylinders with radii  $R_1$  and  $R_2$  rotate with angular velocity  $\Omega_1$  and  $\Omega_2$ .

Following the symmetry of the problem, the projection of the Navier-Stokes equation in cylindrical coordinates gives:

$r$ -projection:

$$\frac{\partial u_r}{\partial t} + (\mathbf{u} \cdot \nabla) u_r - \frac{u_\theta^2}{r} = -\frac{1}{\rho} \frac{\partial p}{\partial r} + \nu (\nabla^2 u_r - \frac{u_r}{r^2} - \frac{2}{r^2} \frac{\partial u_\theta}{\partial \theta}) \quad (7)$$

$\theta$ -projection:

$$\frac{\partial u_\theta}{\partial t} + (\mathbf{u} \cdot \nabla) u_\theta + \frac{u_\theta u_r}{r} = -\frac{1}{\rho r} \frac{\partial p}{\partial \theta} + \nu (\nabla^2 u_\theta - \frac{u_\theta}{r^2} + \frac{2}{r^2} \frac{\partial u_\theta}{\partial \theta}) \quad (8)$$

$z$ -projection:

$$\frac{\partial u_z}{\partial t} + (\mathbf{u} \cdot \nabla) u_z = -\frac{1}{\rho} \frac{\partial p}{\partial z} + \nu (\nabla^2 u_z) \quad (9)$$

where

$$(\mathbf{u} \cdot \nabla) = u_r \frac{\partial}{\partial r} + \frac{u_\theta}{r} \frac{\partial}{\partial \theta} + u_z \frac{\partial}{\partial z} \quad (10)$$

and

$$\nabla^2 = \frac{\partial^2}{\partial r^2} + \frac{1}{r} \frac{\partial}{\partial r} + \frac{1}{r^2} \frac{\partial^2}{\partial \theta^2} + \frac{\partial^2}{\partial z^2} \quad (11)$$

The continuity equation of an incompressible flow in cylindrical coordinates reads:

$$\frac{\partial u_r}{\partial r} + \frac{u_r}{r} + \frac{1}{r} \frac{\partial u_\theta}{\partial \theta} + \frac{\partial u_z}{\partial z} = 0 \quad (12)$$

The fluid rotates between two long concentric cylinders. Neglecting the upper and lower endcaps of the cylinders allows us assume that the velocity has an azimuthal component ( $u_\theta$ ) only, the continuity equation becomes:

$$\frac{\partial u_\theta}{\partial \theta} = 0 \quad (13)$$

The above equation dictates an axi-symmetry of the problem. This symmetry also means:

$$\frac{\partial}{\partial \theta} = 0$$

The projection in the  $r$ -direction reduces to:

$$\frac{u_\theta^2}{r} = \frac{\partial p}{\rho dr} \quad (14)$$

This is a balance between the centrifugal force and the pressure term. Similarly, the projection in the  $\theta$ -direction reduces to:

$$0 = v \left( \frac{\partial^2 u_\theta}{\partial r^2} + \frac{1}{r} \frac{\partial u_\theta}{\partial r} - \frac{u_\theta}{r^2} \right) \quad (15)$$

The above equation is a second order differential equation in  $r$ . The solution is given by:

$$u_{\theta TC}(r) = Ar + \frac{B}{r} \quad (16)$$

where  $A$  and  $B$  are constants determined by the boundary conditions.

The angular velocity is related to  $u_{\theta}$  by

$$\Omega(r) = \frac{u_{\theta}(r)}{r}$$

For the case of TCF:

$$\Omega_{TC}(r) = A + \frac{B}{r^2} \quad (17)$$

To simplify the solution, we introduce dimensionless parameters:

$$\mu_{\Omega} = \Omega_2/\Omega_1$$

and

$$\eta = R_1/R_2$$

We apply the necessary boundary conditions to obtain  $A$  and  $B$ :

- $\Omega(r = R_1) = \Omega_1$
- $\Omega(r = R_2) = \Omega_2$

$$\Rightarrow A = -\Omega_1 \eta^2 \frac{1 - \mu_{\Omega}/\eta^2}{1 - \eta^2} \quad (18)$$

$$\Rightarrow B = \Omega_1 R_1^2 \frac{1 - \mu_{\Omega}}{1 - \eta^2} \quad (19)$$

We have determined the expression of the velocity in the  $\theta$  direction up to the  $0^{\text{th}}$  order. The moving boundary conditions have imposed the expressions on the constants  $A$  and  $B$ . In the next section, we apply the same steps to derive the expression of  $u_{\theta_{TRF}}$  corresponding to the velocity of Thin Rotating Flow in the  $\theta$  direction.

#### D. Base Flow of Thin Rotating Flow (TRF)

We study the laminar flow of a thin layer of viscous fluid subject to an external Lorentz force in the azimuthal direction  $\mathbf{f} = \mathbf{j} \times \mathbf{B}$  in a fixed cylindrical container.

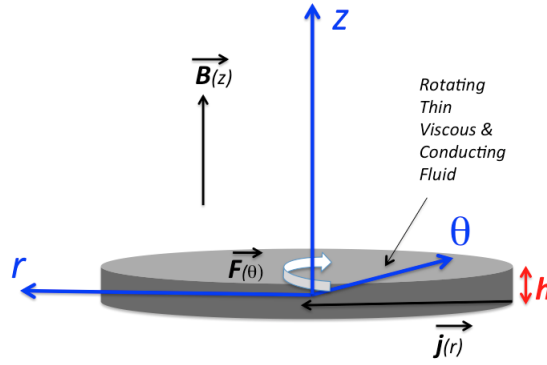


Figure 13: Schematic drawing of Thin Rotating Flow. A thin layer of a viscous and conducting fluid is situated in an axial magnetic field  $\mathbf{B}$  and a radial current density  $\mathbf{j}$ . The resulting Lorentz force,  $\mathbf{f} = \mathbf{j} \times \mathbf{B}$ , in the azimuthal direction rotates the fluid.

The magnetic field is axial with an expression of  $\mathbf{B} = (0, 0, B_0 \hat{\mathbf{z}})$ . The height of the fluid is denoted by  $z$ . The current density,  $\mathbf{j} = j \hat{\mathbf{r}}$ , where  $j$  is the ratio of total current  $I$  and the area  $A(r) = 2\pi zr$ .

$$\mathbf{j}(r) = \frac{I}{2\pi z} \frac{1}{r} \hat{\mathbf{r}} \quad (20)$$

In cylindrical coordinates  $(r, \theta, z)$ , the projection of Navier-Stokes equations in the  $\theta$ -direction along with the external Lorentz force is given by:

$$\frac{\partial u_\theta}{\partial t} + (\mathbf{u} \cdot \nabla) u_\theta + \frac{u_\theta u_r}{r} = -\frac{1}{\rho r} \frac{\partial p}{\partial \theta} + \nu \left( \nabla^2 u_\theta - \frac{u_\theta}{r^2} + \frac{2}{r^2} \frac{\partial u_\theta}{\partial \theta} \right) + \frac{j(r) B_0}{\rho} \quad (21)$$

Assuming  $u_r = 0$  and  $u_z = 0$ , and supposing that the variations in the angular and vertical motion are negligible, ( $\partial/\partial\theta = 0$ , and  $\partial/\partial z = 0$ ) we can reduce the projection in the  $\theta$  direction to obtain a non homogeneous second order differential equation of non-constant coefficients of the form:

$$\frac{\partial^2 u_\theta}{\partial r^2} + \frac{1}{r} \frac{\partial u_\theta}{\partial r} - \frac{u_\theta}{r^2} = -\frac{j(r) B_0}{\mu} \quad (22)$$

where  $\mu = \nu\rho$ . Let  $\alpha = -IB_0/2\pi z\mu$ . The solution of the differential equation is given by:

$$u_\theta = Gr + \frac{F}{r} - \frac{\alpha}{2} r \ln(r) \quad (23)$$

$$u_\theta/r = \Omega:$$

$$\Omega_{TRF} = G + \frac{F}{r^2} - \frac{\alpha}{2} \ln(r) \quad (24)$$

where  $G$  and  $F$  are constants determined by boundary conditions. The cylindrical container in TRF is not rotating. As a consequence, the velocities at the boundaries vanish. Let  $a$  be the radius of the middle electrode, and  $R$  be the radius of the cylinder, the boundary conditions are given by:

(1) At  $r = a$ , we have

$$u_{\theta} = Ga + \frac{F}{a} - \frac{\alpha}{2}a \ln(a) = 0 \quad (25)$$

(2) At  $r = R$ , we have

$$u_{\theta} = GR + \frac{F}{R} - \frac{\alpha}{2}R \ln(R) = 0 \quad (26)$$

With  $\eta = R/a$  we obtain:

$$G = \frac{\alpha}{2} \left\{ \frac{\eta^2 \ln(a) - \ln(R)}{\eta^2 - 1} \right\} \quad (27)$$

and

$$F = \frac{\alpha}{2} \left\{ \frac{a^2 \ln(\eta)}{1 - \eta^2} \right\} \quad (28)$$

The solution of the velocity profile is dependent on the value of  $\alpha$ . In other words, it is dependent on the magnetic field  $B$ , current density  $j$ , density  $\rho$  as well as the dynamic viscosity of the fluid  $\mu$ . The plot of velocity profile for several values of electric current is shown in Fig.(14). The form of the velocity is nearly parabolic vanishing at the boundaries  $a$  and  $R$ . The highest magnitude of the velocity is reached where  $r/a$  is almost 8 independently of the magnitude of the current. The magnitude of velocity increases with increasing current.

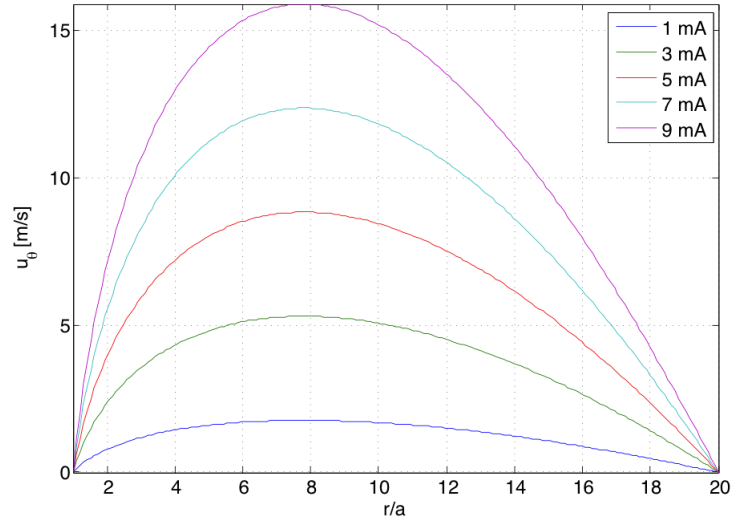


Figure 14: Velocity profiles versus normalized radius for several values of the electric current ( $\alpha = 150, 450, 750, 1000, 135$ ). As the current density increases, the maximum value of the velocity increases.

### E. Comparison Between TCF and TRF

In this section, we highlight the differences between the TCF and TRF setups. The origin of rotation of the fluid in the TRF is the Lorentz force, whereas the origin of rotation in TCF experiment is the rotation of the two concentric cylinders. In TCF, the non-vanishing boundary conditions are caused by the rotations  $\Omega_1$  and  $\Omega_2$  of the inner and outer cylinders. In TRF, the cylinder is fixed forcing vanishing boundary conditions.

In the TRF setup, the fluid height is kept small to promote the growth of the two dimensional non-axisymmetric instability in the  $(r, \theta)$ -plane. On the contrary, the fluid in TCF height is taken to be large as compared to that of the radius of the outer cylinder to promote the instability in the  $(r, z)$ -plane. Table (1) summarizes these ideas. The velocities of TRF and TCF are plotted versus normalized radius  $r/a$  in Fig.(15).



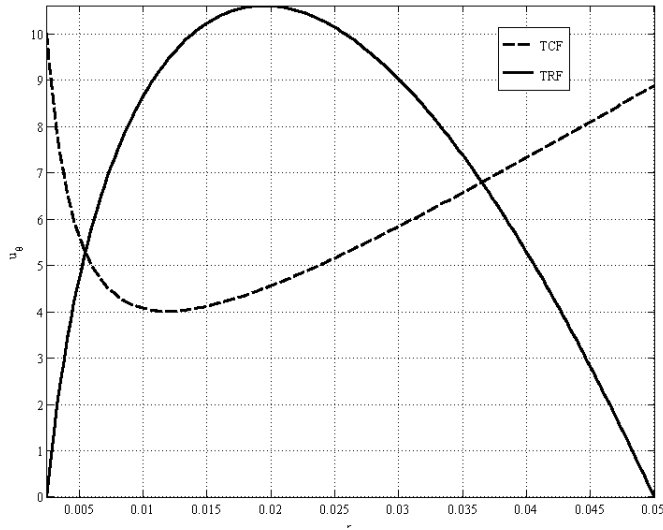


Figure 15: Comparison of velocity profiles for TCF and TRF in arbitrary units. In the TC flow,  $\Omega_1 = 4000s^{-1}$  and  $\Omega_2 = 533/2s^{-1}$  according to one of the PRINCETON experiments. In TRF  $\alpha = 3$ .

Table 1: Comparison between TCF and TRF

Taylor-Couette Flow	Magnetized Shallow Rotating Flow
Thick layer of fluid	Thin layer of conducting fluid
Promotes TCI in $(r, z)$	Suppresses TCI in $(r, z)$
Studies MRI in $(r, z)$	Studies 2D-NACI in $(r, \theta)$
Moving boundaries	Fixed boundaries
Fluid rotation due to the rotation of the cylinders ( $\Omega_1$ and $\Omega_2$ )	Fluid rotation due to Lorentz force

## F. Conclusion

In this chapter, the  $0^{th}$  order velocity of the TCF and TRF are derived using the Navier-Stokes equations and the continuity equation in cylindrical coordinates. The necessary boundary conditions are applied to obtain the full expression of velocity. We will see that the base flow is a key element in the study of stability of the flow. In the end the, velocities of both flows were plotted and compared. Below are the results of the derivation of angular velocity:

$$\Omega_{TC}(r) = A + \frac{B}{r^2}, \quad (29)$$

$$\Omega_{TRF} = G + \frac{F}{r^2} - \frac{\alpha}{2} \ln(r). \quad (30)$$

# CHAPTER III

## STABILITY ANALYSIS

## A. Introduction

The primary purpose of this research work is to explore the behavior of a system of rotating flow around its equilibrium state. In simple words, the way to study the stability of the rotating fluid is to give its equilibrium state a small kick and analyze whether the system goes back to its stable position or escapes into an unstable orbit as time evolves. This is a simplified description of what is called perturbation theory.

Perturbation theory leads to an expression of the perturbed quantity in terms of a small parameter, or the kick that we have mentioned earlier, known as perturbation series. This term quantifies the deviation from the exactly solvable problem. The leading term in this power series is the exact solution of base flow, while the other terms describe the deviation in the solution from the initial problem. Fig.(16) shows the difference between a stable and an unstable equilibrium.



Figure 16: (a) A perturbation to the system in a stable equilibrium results in the return to the stable position. (b) A perturbation in the unstable equilibrium results in the escape away from stable position.

In this chapter, we study the stability of a thin rotating fluid subject an external Lorentz force by applying perturbation theory.

The instability of rotating flows was first considered by Rayleigh. He considered

a basic swirling flow of an inviscid fluid rotating with an angular velocity  $\Omega(r)$ . Rayleigh's circulation criterion states that a necessary and sufficient condition for the stability of a flow to axisymmetric disturbances is that the square of the circulation does not decrease anywhere [6]. In other words, he states that  $\Phi \geq 0$  everywhere in the field of the flow, where  $\Phi$  is the Rayleigh discriminant defined by:

$$\Phi = \frac{1}{r^3} \frac{d}{dr} (r^2 \Omega)^2 \quad (31)$$

## B. Axisymmetric Disturbances of Taylor-Couete Flow

In this section, we discuss the argument behind Rayleigh's criterion for the stability of Couette flow. Navier-Stokes equations in cylindrical coordinates  $(r, \theta, z)$  neglecting the viscous effects can be written as:

$$\frac{Du_r}{Dt} - \frac{u_\theta^2}{r} = -\frac{1}{\rho} \frac{\partial p}{\partial r} \quad (32)$$

$$\frac{Du_\theta}{Dt} + \frac{u_\theta u_r}{r} = -\frac{1}{\rho} \frac{1}{r} \frac{\partial p}{\partial \theta} \quad (33)$$

$$\frac{Du_z}{Dt} = -\frac{1}{\rho} \frac{\partial p}{\partial z} \quad (34)$$

$$\frac{D}{Dt} = \frac{\partial}{\partial t} + u_r \frac{\partial}{\partial r} + \frac{u_\theta}{r} \frac{\partial}{\partial \theta} + u_z \frac{\partial}{\partial z} \quad (35)$$

These equations allow for a steady basic solution of the form  $u_r = u_z = 0$  and  $u_\theta = u_{\theta_0}$  where  $u_{\theta_0} = r\Omega$  is the azimuthal velocity determined by the solution of the base flow. The pressure distribution is given by:

$$p_0(r) = \rho \int \frac{u_{\theta_0}^2}{r} dr \quad (36)$$

To study the stability of the steady flow given by the above conditions, we seek to distinguish between stable and unstable distributions of basic angular velocity.

Rayleigh first considered axisymmetric disturbances by setting

$$\partial/\partial\theta = 0$$

The equations are then reduced to

$$\frac{D'u_r}{Dt'} - \frac{u_{\theta}^2}{r} = -\frac{1}{\rho} \frac{\partial p}{\partial r} \quad (37)$$

$$\frac{D'u_{\theta}}{Dt'} + \frac{u_{\theta}u_r}{r} = 0 \quad (38)$$

$$\frac{D'u_z}{Dt'} = -\frac{1}{\rho} \frac{\partial p}{\partial z} \quad (39)$$

$$\frac{D'}{Dt'} = \frac{\partial}{\partial t} + u_r \frac{\partial}{\partial r} + u_z \frac{\partial}{\partial z} \quad (40)$$

and the continuity equation reduces to

$$\frac{\partial u_r}{\partial r} + \frac{u_r}{r} + \frac{\partial u_z}{\partial z} = 0 \quad (41)$$

The reduced equation in the  $\theta$ -direction can be written in the form

$$\frac{\partial u_{\theta}}{\partial t} + \frac{u_{\theta}u_r}{r} = r \frac{\partial u_{\theta}}{\partial t} + u_{\theta} \frac{\partial r}{\partial t} = \frac{d}{dt}(ru_{\theta}) = \frac{d}{dt}(r^2\Omega) = 0$$

By Kelvin's circulation theorem, one can see from the above equation, that the angular momentum  $L = r^2\Omega$  of a fluid element per unit of mass is conserved.

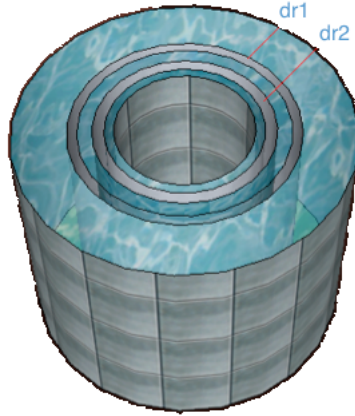


Figure 17: Sketch of Taylor-Couette Flow, An interchange of fluid between two rings means a change in angular momentum.

Since  $L$  is a constant of motion, we associate with this force a potential energy:

$$E_p = \frac{\rho L^2}{2r^2}$$

If we take two elementary rings of equal heights and masses at  $r = r_1$  and  $r = r_2$ , the equality of their masses requires:

$$2\pi r_1 dr_1 = 2\pi r_2 dr_2 = dS$$

If we interchange the fluid contained in  $dr_1$  and  $dr_2$ , the change in kinetic energy is equal to the change in potential energy because the angular momentum is conserved. Therefore, the change in kinetic energy is proportional to:

$$E_k \propto \left\{ \left( \frac{L_2^2}{r_1^2} + \frac{L_1^2}{r_2^2} \right) - \left( \frac{L_1^2}{r_1^2} + \frac{L_2^2}{r_2^2} \right) \right\} dS = (L_2^2 - L_1^2) \left( \frac{1}{r_1^2} - \frac{1}{r_2^2} \right) dS$$

If  $r_2 > r_1$ , one can see that this is a positive quantity for  $L_2^2 > L_1^2$  and negative for  $L_2^2 < L_1^2$ . If  $L^2$  is monotonically increasing with  $r$ , there will be no possible interchange of fluid on the rings as we have imagined without a source of energy, this signifies a stable flow. If  $L^2$  is monotonically decreasing with  $r$ , then the interchange of fluid on the rings will result in a liberation of energy, this indicated the existence of an instability.

It must be emphasized that if  $L^2$  is non-decreasing then the inference of stability applies only to axisymmetric disturbances. Furthermore, the flow might be unstable to other types of disturbances.

For a general base flow angular velocity  $\Omega$ , such as the form that we have determined in the previous chapter for thin rotating flow with external Lorentz force, Rayleigh criterion is known to be invalid for non-axisymmetric disturbances. Howard and Gupta have studied the non-axisymmetric case and concluded that no general stability criterion was determined [30].

### **C. Non-Axisymmetric Disturbances by Slab Approximation (TRF)**

The application of axisymmetric disturbances, studied by many authors (Chandrasekhar [31], Howard and Gupta [30], Balbus and Hawely [16], and H. Ji et al. [32]), corresponds to the introduction of a perturbed term of the velocity of a fluid while assuming there are no variations in the angular direction ( $\partial/\partial\theta = 0$ ). In this section, we introduce a non-axisymmetric disturbance to the azimuthal component of the velocity of the flow and analyze the obtained dispersion relation.



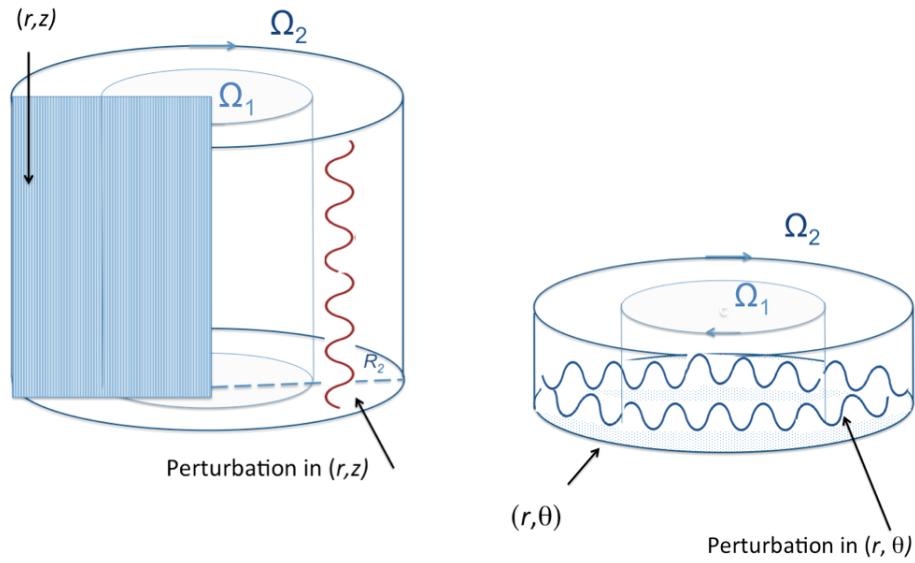


Figure 18: Left. Axisymmetric Disturbances in the  $(r, z)$ -plane. Right. Nonaxisymmetric Disturbances in the  $(r, \theta)$ -plane.

The slab approximation method is characterized by a transformation between the cylindrical coordinates  $(r, \theta, z)$  and the Cartesian coordinates  $(x, y, z)$ . In this method,  $r$  is transformed into  $x$ , and  $\theta$  is transformed into  $y$ . In the remaining part of this chapter, we use Cartesian coordinates of Navier Stokes equations. Fig.(19) shows the relation between the two systems of coordinates. The determination of instability in the  $(r, \theta)$  plane for the magnetized rotating flow is performed by applying nine steps that we outline as follows:

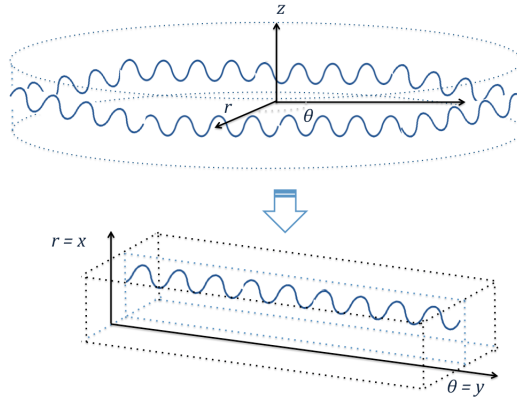


Figure 19: Slab Approximation. The  $r$ -direction is becomes the  $x$  coordinate, and the  $\theta$ -direction becomes the  $y$  coordinate.

### 1. Full Navier-Stokes Equations with Lorentz Force

We begin with writing the full Navier-Stokes Equations in Cartesian Coordinates with viscosity and external Lorentz force only in the  $y$  direction:

$$\frac{\partial u}{\partial t} + u \frac{\partial u}{\partial x} + v \frac{\partial u}{\partial y} + w \frac{\partial u}{\partial z} = -\frac{1}{\rho} \frac{\partial p}{\partial x} + \nu \left( u \frac{\partial^2 u}{\partial x^2} + v \frac{\partial^2 u}{\partial y^2} + w \frac{\partial^2 u}{\partial z^2} \right) \quad (42)$$

$$\frac{\partial v}{\partial t} + u \frac{\partial v}{\partial x} + v \frac{\partial v}{\partial y} + w \frac{\partial v}{\partial z} = -\frac{1}{\rho} \frac{\partial p}{\partial y} + \nu \left( u \frac{\partial^2 v}{\partial x^2} + v \frac{\partial^2 v}{\partial y^2} + w \frac{\partial^2 v}{\partial z^2} \right) + \frac{jB}{\rho} \quad (43)$$

$$\frac{\partial w}{\partial t} + u \frac{\partial w}{\partial x} + v \frac{\partial w}{\partial y} + w \frac{\partial w}{\partial z} = -\frac{1}{\rho} \frac{\partial p}{\partial z} + \nu \left( u \frac{\partial^2 w}{\partial x^2} + v \frac{\partial^2 w}{\partial y^2} + w \frac{\partial^2 w}{\partial z^2} \right) \quad (44)$$

Continuity equation is given by

$$\frac{\partial u}{\partial x} + \frac{\partial v}{\partial y} + \frac{\partial w}{\partial z} = 0 \quad (45)$$

where  $(u, v, w)$  are the velocity components in Cartesian coordinates.

## 2. Form of Perturbation

Next, we consider an infinitesimal perturbation of the basic flow. This perturbation is non-axisymmetric and two dimensional since the height of the fluid is very small as compared to its diameter. We describe the perturbed flow in the  $(x, y)$  direction by

$$\mathbf{u} = \begin{cases} \tilde{u}(x, y, t) \\ v_0 + \tilde{v}(x, y, t) \\ 0 \end{cases} \quad (46)$$

$$p = p_0 + \tilde{p}(x, y, t) \quad (47)$$

where the steady base flow solution is given by  $u = w = 0$ ,  $p = p_0$  and  $v = v_0$

## 3. Steady State and Inviscid Limit

From  $0^{th}$  order in the  $r$  direction, that we have derived in the previous chapter, we have the equality of the following terms,

$$\frac{(u_\theta)^2}{r} = \frac{1}{\rho} \frac{\partial p_0}{\partial r} \quad (48)$$

Then we can drop the term  $p_0$ .

Similarly, from  $0^{th}$  order in the  $\theta$  direction, we have the equality of the following terms,

$$v(\nabla^2 u_\theta - \frac{u_\theta}{r^2} + \frac{2}{r^2} \frac{\partial u_\theta}{\partial \theta}) = -\frac{j(r)B_0}{\rho} \quad (49)$$

Therefore, the force cancels out with the viscosity term.

#### 4. Linearization

Performing a linearization significantly simplifies the problem. By dropping second order terms, we still obtain an expression which is rich with information about the stability of the flow up to the first order.

The linearized equations are given by:

*Linearized x direction:*

$$\frac{\partial \tilde{u}}{\partial t} + v_0 \frac{\partial \tilde{u}}{\partial y} = -\frac{1}{\rho} \frac{\partial \tilde{p}}{\partial x} \quad (50)$$

*Linearized y direction:*

$$\frac{\partial \tilde{v}}{\partial t} + \frac{\partial v_0}{\partial x} \tilde{u} + v_0 \frac{\partial \tilde{v}}{\partial y} = -\frac{1}{\rho} \frac{\partial \tilde{p}}{\partial y} \quad (51)$$

#### 5. Pressure Elimination and Coupling by Continuity

A common trick to reduce the above two equations of two unknowns ( $\tilde{u}$  and  $\tilde{v}$ ) to one equation of two unknowns is to apply the vorticity equation; ( $\partial/\partial y$  of  $x$ - direction -  $\partial/\partial x$   $y$ -direction). With this method, the pressure dependency can be removed.

$$\begin{aligned} & \frac{\partial}{\partial t} \left[ \frac{\partial \tilde{u}}{\partial y} - \frac{\partial \tilde{v}}{\partial x} \right] \\ & + v_0 \frac{\partial^2 \tilde{u}}{\partial y^2} - \frac{\partial}{\partial x} \left( \tilde{u} \frac{\partial v_0}{\partial x} \right) - \frac{\partial}{\partial x} \left( v_0 \frac{\partial \tilde{v}}{\partial y} \right) = 0 \end{aligned}$$

To reduce the above equation of one equation of two unknowns ( $\tilde{u}$  and  $\tilde{v}$ ), to one equation of one unknown ( $\tilde{u}$ ) is through the continuity equation.

The reduced linearized form of continuity:

$$\frac{\partial \tilde{u}}{\partial x} + \frac{\partial \tilde{v}}{\partial y} = 0 \quad (52)$$

### 6. Fourier Modes Analysis

In accordance with the general procedure of treating these problems, we analyze the disturbance into normal modes. In the present instance, it is natural to suppose that the various quantities describing the perturbations have a  $(x, y, t)$  dependence given by:

$$\tilde{u}(x, y, t) = \bar{u}(x)e^{imy - i\omega t} \quad (53)$$

$$\tilde{v}(x, y, t) = v(x)e^{imy - i\omega t} \quad (54)$$

where  $u(x)$  and  $v(x)$  are arbitrary functions of  $x$ ; they represents amplitude of the normal modes.

Applying Fourier Modes to continuity equation, we obtain:

$$\tilde{v} = \frac{i}{m} \frac{\partial \tilde{u}}{\partial x} \quad (55)$$

Applying Fourier Modes to the resultant of the pressure elimination equation and replacing  $(\tilde{v})$  by its equivalent from continuity equation, we obtain the following dispersion relation.

$$m\omega + m^{-1}\ddot{u}\omega - m^2v_0u - \ddot{v}_0u + v_0\ddot{u} = 0 \quad (56)$$

where  $\ddot{u} = \partial^2 u / \partial x^2$  and  $\ddot{v}_0 = \partial^2 v_0 / \partial x^2$

Solving for  $\omega$ , we obtain a dispersion relation:

$$\omega = \frac{m^2 v_0 u + \ddot{v}_0 u - v_0 \ddot{u}}{m u + m^{-1} \ddot{u}} \quad (57)$$

### 7. Stability Conditions

The wavenumber  $\omega$  is a function of  $m$ . If  $m$  is real, then  $\omega$  is real. If  $\omega = 0$ , then  $m$  can be complex. The expression of  $m^2$  is given by:

$$m^2 = \frac{-\ddot{v}_0 u + v_0 \ddot{u}}{v_0 u} = \frac{-\ddot{v}_0 - v_0 k_x^2}{v_0} \quad (58)$$

According to the above expression,  $m^2$  depends to the form of  $u$ . The boundary conditions characterized by fixed walls force the velocity  $u$  to take a certain form that vanishes at  $r = a$  and  $r = R$ . Let us suppose that:

$$u(x) = \sin(k_x x)$$

where  $k_x = n\pi/R$  then,

$$\ddot{u}(x) = -k_x^2 \sin(k_x x) = -k_x^2 u$$

Since  $v_0$  is always positive, the sign of  $m^2$  is governed by the numerator. If the numerator is negative, then  $m^2$  is imaginary and  $\exp(imy)$  is a an oscillatory function. The flow in this case is stable. However, if the numerator is positive, then  $m^2$  is real and  $\exp(imy)$  could be an exponentially growing function. In this case, the flow is unstable. This is summarized in Fig.(20)

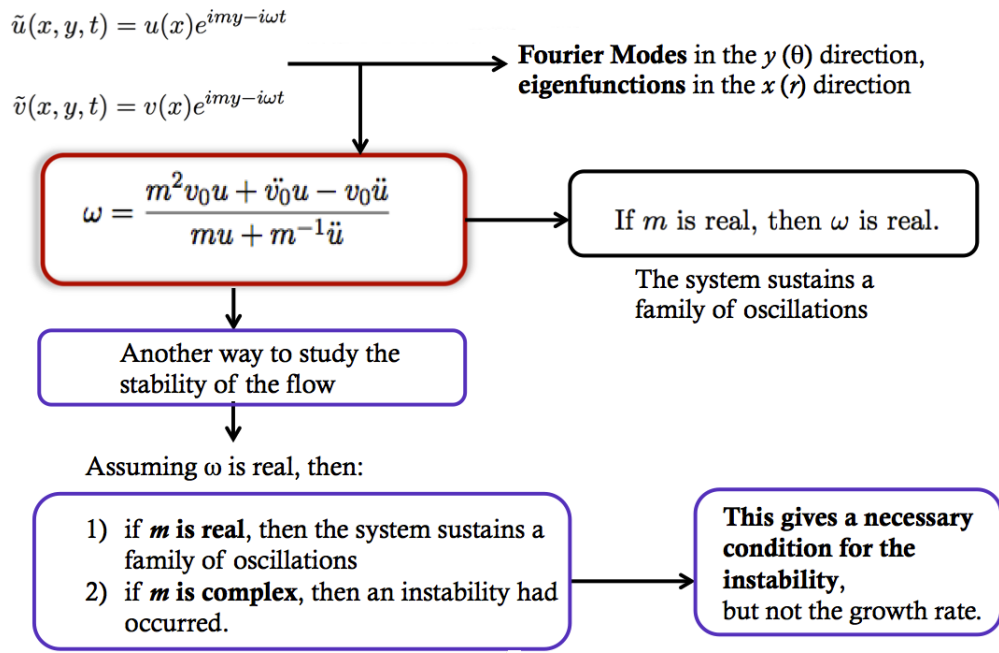


Figure 20: The methodology of analyzing the dispersion relation

To explore the behavior of  $m^2$  for  $n = 1, 2, 3, 4$ , and  $5$ , we plot  $m^2$  versus  $r/a$  as shown in Fig. 21. The form of  $m^2$  is parabolic in shape starting with a high positive magnitude until it reaches a particular value  $r_a$ . For  $r_a < r/a < r_R$ ,  $m^2$  is negative with the highest negative value at  $r/a$  is  $8$ . For  $r_R < r/a < 20$ ,  $m^2$  becomes slightly positive. As  $n$  decreases  $r_a$  increases and  $r_R$  decreases. The same trend occurs for all values of  $n$ . To understand the variation of  $m^2$  with increasing total current, we plot  $m^2$  versus  $r/a$  for several currents ( $I = 2, 4, 6$  and  $8$  A) at  $n = 2$ . The form of  $m^2$  is parabolic in shape starting with a high positive magnitude until it reaches a particular value  $r_{I1} = 3.7$  at all values of  $I$ . For  $r_{I1} < r/a < r_{I2}$ ,  $m^2$  is negative. The value of  $r_{I2} = 19.5$  for all  $I$ . For  $r > r_{I2}$ ,  $m^2$  The same trend occurs for all values of  $n$ .

According to Fig.(21),  $m^2$  is more negative towards the central electrode. This indicates that the flow is unstable in this region. It is shown that  $m^2$  is positive near  $r = a$

and  $r = R$  indicating a relatively small stable zone. Furthermore, one can deduce that the unstable region expands as  $n$  increases. This implies that the higher the oscillations of  $u(x)$ , the more unstable the flow is. According to Fig.(22),  $m^2$  is more negative towards the central electrode. One can deduce that the unstable region doesn't vary as function of current.

The previous interpretation is open to modifications and further analysis. We have based our interpretation on a particular form of the amplitude of the amplitude. Many other forms of  $u(x)$  are also valid. In reference to the interpretation done by Balbus in Ref.([33]), we have analyzed the spatial perturbation of the flow and obtained conditions of stability according to the waves in the spatial direction  $y$ . We haven't obtained a temporal expression of the complex component of  $\omega$ . Therefore, we do not predict the evolution of the perturbation with time.

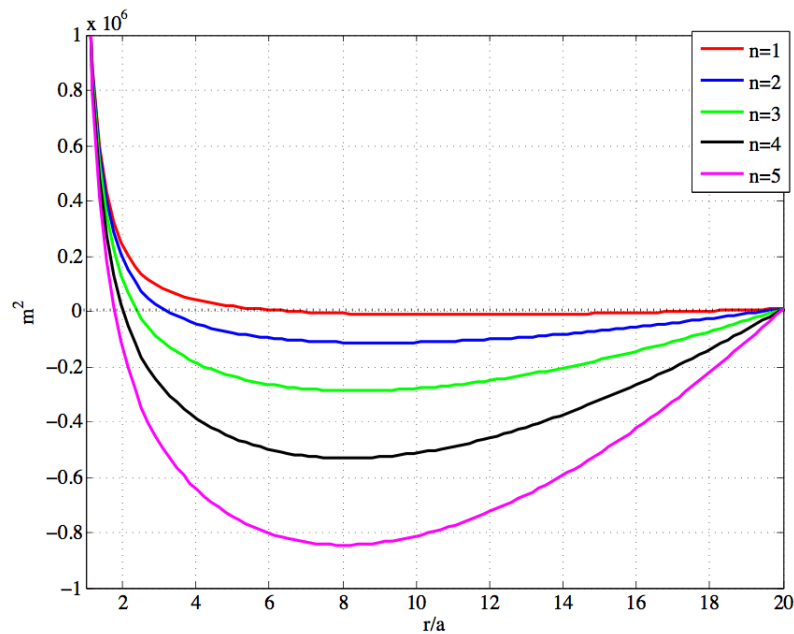


Figure 21: Plot of  $m^2$  versus  $r/a$  for  $n = 1, 2, \dots, 5$  for  $I = 1$  A.



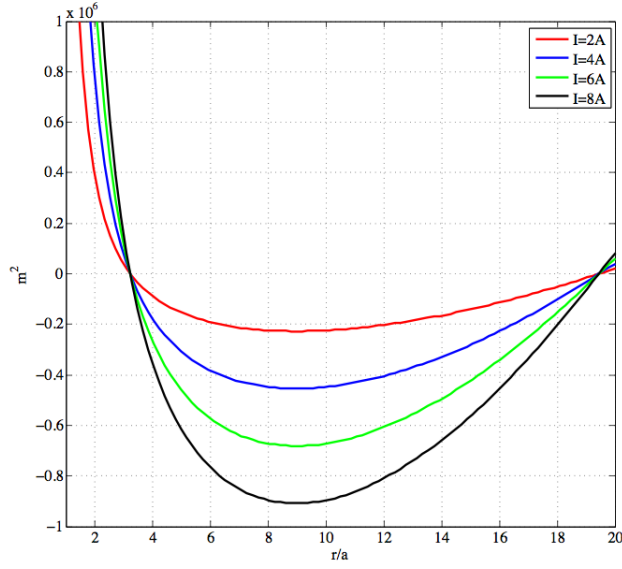


Figure 22: Plot of  $m^2$  versus  $r/a$  for  $I = 2, 4, 6,$  and  $8$  A for  $n = 2$ .

#### D. Conclusion

In this chapter, the dynamics of the flow are investigated. For TCF, we study Rayleigh criterion with axisymmetric disturbance. The stability of TRF is studied by perturbation theory in a slab geometry. First, non-axisymmetric disturbances of exponential dependence are applied to the velocity of the base flow. Using linearized Navier-Stokes equations, the motion in the inviscid limit is studied. Applying the vorticity equation eliminates the pressure dependence. By using Fourier modes, a dispersion relation is determined in terms of the wavenumber in the  $y$ -direction. In accordance with boundary conditions, the radial velocity is assumed to have a sinusoidal form with a wavenumber  $k_x = n\pi/R$ . The variations of  $m^2$  versus normalized radius for several values of  $n$  are plotted. Analysis of the plot allows us to conclude:

- The flow is conditionally unstable.

- The region near the central electrode is unstable.
- The region in the middle of the cylindrical container is stable.
- The region near the outer electrode is unstable.
- The onset of instability versus radius is independent of current.
- The unstable region increases with increasing  $n$ .

CHAPTER IV  
THE EXPERIMENT AND LASER DIAGNOSTIC

## A. Introduction

In this thesis, a tabletop experiment is designed to investigate the properties of the fluid motion in a thin rotating flow. Instabilities in rotating flows are studied in axially magnetized Taylor-Couette experiments in cylindrical geometry such that the instability develops in the  $(r, z)$ -plane [34, 35]. They are also studied in Taylor-Couette experiments with helical magnetic field such that the instability develops in the  $(r, \theta)$  plane as shown in Fig.(23). Unlike magnetized Taylor-Couette experiments, we aim at suppressing the conventional instability by reducing the height of the fluid to few millimeters. This promotes the growth of the a hydrodynamic instability in the  $(r, \theta)$ -plane.

In this chapter, we introduce the experimental setup. We describe the fluid characteristics, the external magnetic field applied to the fluid, the current density inside the fluid, and the induced magnetic field due to the rotation of the fluid. At this stage, we aim at studying the flow experimentally. We design an experimental procedure to obtain the velocity variations in the fluid motion. The measurements which are collected from the experiment are linked to the velocity components via a set of equations called Shallow Water Equations.

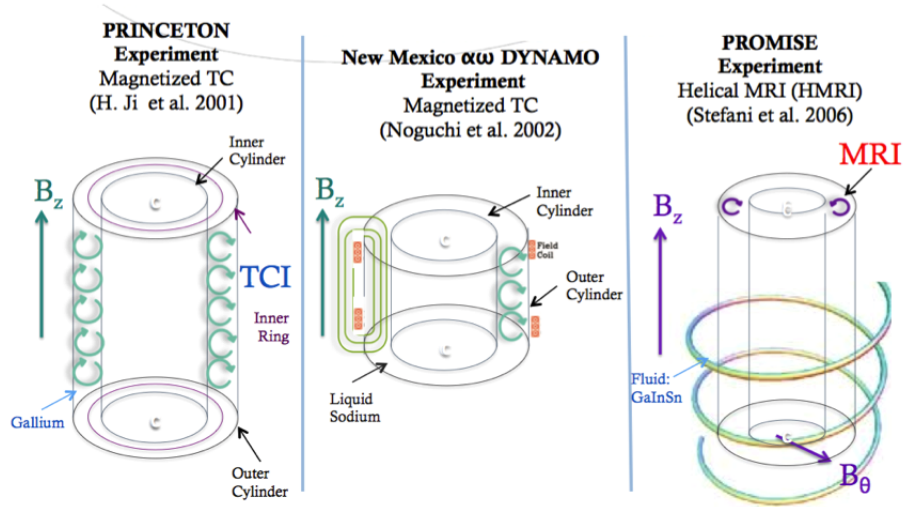


Figure 23: Instabilities were studied in magnetized Taylor-Couette apparatus with axial magnetic field in Ref.[32, 36]. In the  $\alpha\omega$  Dynamo experiment, the instability is also studied in the  $(r, z)$ -plane using liquid sodium. In the Promise experiment, a helical magnetic field leads to the development of the instability.

## B. The Experimental Apparatus

A thin layer of liquid metal is placed in a cylindrical Plexiglas container. The side wall of the container is grooved to install eight stainless-steel electrodes, of diameter 5 mm and height 5 cm each. The dimensions of the experimental setup are listed in table (2). The electrodes are all connected to the negative terminal of a power supply. At the center of the container, another electrode is installed and connected to the ground terminal of the power supply. A photograph of the experiment is shown in Fig.(24).

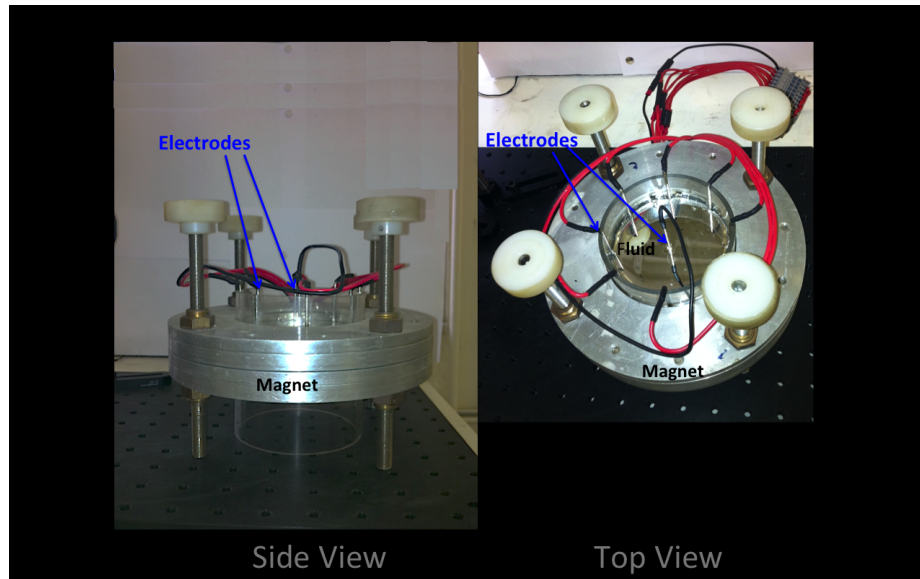


Figure 24: Experimental setup of rotating liquid metal. Eight outer electrodes are installed on the outer wall of a cylindrical container. A middle electrode is installed in the center of the container. The container is placed inside a set of two permanent magnets which generate an axial magnetic field.

The container is placed in the middle of a set of two permanent magnets providing a magnetic field the axial direction which is discussed in the next section. As the power supply is switched on, the outer electrodes are biased with respect to the inner electrode, allowing for an electric current to flow inside the fluid in the radial direction. With the magnetic field in the axial direction and the electric current in the radial direction, a Lorentz force is generated in the  $\theta$  direction. The fluid starts to rotate as soon as the power supply is switched on.

### C. Fluid Characteristics

The fluid used in the experiment is Galinstan . It is an alloy of (Gallium (Ga), Indium (In) and Tin(Sn)). It is a non toxic liquid metal, easier to manipulate than mercury which is highly toxic and has a high vapor pressure. It is also better to use than lithium

Table 2: Setup Dimensions

Property	Value
Outer Cylinder Radius (R)	50 mm
Inner Cylinder Radius (a)	2.5 mm
Height of the Fluid (h)	5 mm
Gap Width (w)	$R - 2a = 45$ mm
Aspect Ratio ( $\Gamma$ )	$\Gamma = H/(R - a) = 0.1$
Radius Ratio ( $\eta$ )	$\eta = a/R = 0.05$

and sodium, which are reactive with water. Galinstan is not chemically reactive like liquid Gallium. Its melting point is  $-19^{\circ}\text{C}$ . It is compatible with most metals and plastics. Its viscosity is almost one third the viscosity of water. Galinstan is six times denser than water and  $10^{10}$  times more electrically conductive. Its surface tension is five times that of water. Galinstan is characterized by a reflective shining surface as shown in Fig. (25). When GaInSn is exposed to oxygen, it slowly oxidizes to form a protective layer of  $\text{Ga}_2\text{O}_3$  on its surface [37]. This layer is carefully removed during the process of collecting measurements. Properties of Galinstan and water are given in table (3).

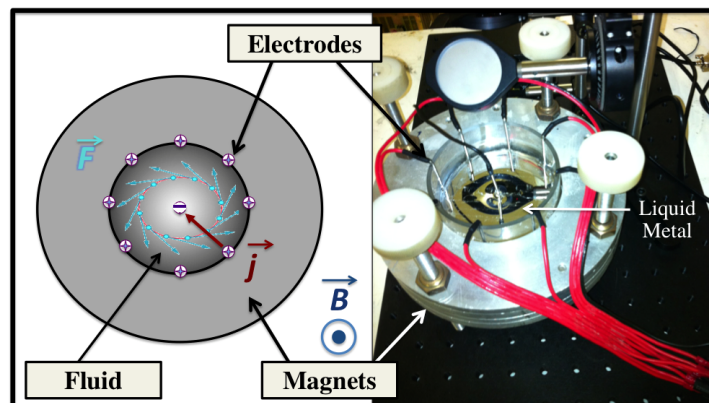


Figure 25: Rotating Galinstan in a cylindrical container under the effect of Lorentz force.

Table 3: Properties of Galinstan and Water

Composition	Ga <sup>67</sup> In <sup>20.5</sup> Sn <sup>12.5</sup>	Water
Viscosity (m <sup>2</sup> s <sup>-1</sup> )	$2.98 \times 10^{-7}$	$8.9 \times 10^{-7}$
Density (Kg m <sup>-3</sup> )	6360	1000
Surface Tension (Nm <sup>-1</sup> )	0.533	0.073
Electric Conductivity ( $\Omega^{-1}\text{m}^{-1}$ )	$3.1 \times 10^6$	$10^{-4}$
Melting Temperature (°C)	-19	0

#### D. External Magnetic Field

The cylindrical container is placed in the middle of two axially magnetized Neodymium ring magnets, each of inner diameter 10 cm of thickness 2 cm. The two magnets are held together through screws to control the separation between them. During the experiment, they are tightly squeezed such that the separation is 4 mm. Using a teslameter equipped with a probe based on Hall Effect as shown in Fig.(26), we measure the external magnetic field. In these measurements, the axis perpendicular to the probe is taken to be the  $r$ -direction, while the axis parallel to the probe is taken to be the  $z$ -direction.



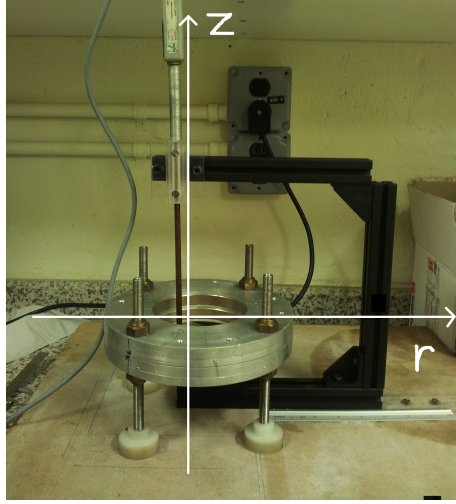


Figure 26: Two ring magnets provide the external magnetic field. Measuring the external magnetic field using teslameter based on Hall Effect.

In the measurements reported in Fig.(27), the magnetic field is measured versus the  $r$ -direction. The curve of magnetic field is parabolic starting with -200 mT near the outer electrodes. The magnitude of the field decreases to reach a minimum of -90 mT at the center (around  $r/a= 9$ ). A curve fit is applied to the experimental data so that a polynomial as function of  $r$  is obtained:

$$B(r) = -7r^2 + 70r - 258 \quad (59)$$

The measurements reported in Fig.(28) correspond to the magnetic field versus the  $z$  direction at four radial positions denoted by  $r_0, r_1, r_2, r_3$ , and  $r_4$ , such that the distance between two consecutive positions is 1 cm. The curve of the field is parabolic with its lowest value,  $B_{max}$ , at the center of the two magnets. The minimum value  $B_{min}$  mT is near the boundaries. A thin layer of Galinstan of thickness 5 mm is poured in the container at height  $z$  corresponding to  $B = -90$  mT.

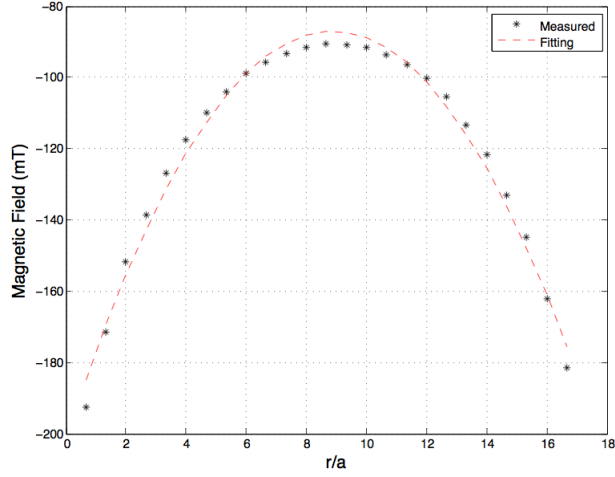


Figure 27: Magnetic field measurements and a polynomial fit.

## E. Current Density

In this section, we determine the expression of current density in the flow.

Consider two concentric conducting cylinders with radii ( $R < a$ ) such that the space between the two conductors is filled with a fluid with resistivity  $\rho_e$ . If we consider the current passing through a sequence of cylindrical shells of radius  $r$  and thickness  $dr$ , then each shell has a resistance  $dR$  given by:

$$dR = \frac{\rho_e}{2\pi z} \frac{dr}{r} \quad (60)$$

Integrating from  $r = a$  and  $r = R$  to find the total resistance, we obtain:

$$R(r) = \int_a^R dR = \int_a^R \frac{\rho_e}{2\pi z} \frac{dr}{r} = \frac{\rho}{2\pi z} \ln\left(\frac{r}{a}\right) \quad (61)$$

The current density is the total current  $I$  per unit area, therefore,  $j$  at a distance  $r$  from the center can be written as :

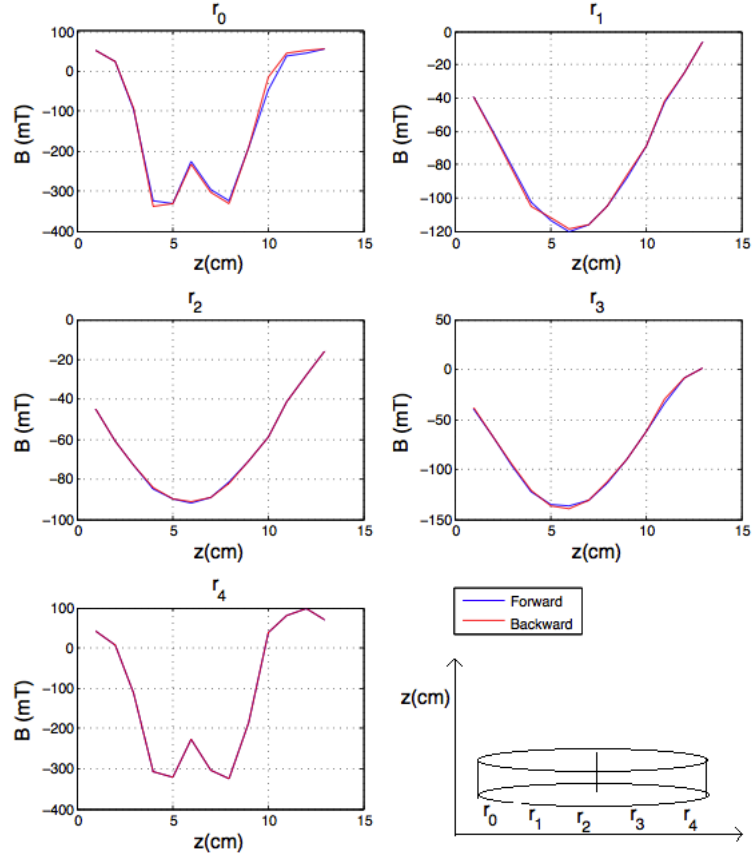


Figure 28: Plot of magnetic field versus height for four different positions inside the inner diameter of the permanent magnets  $r_0, r_1, r_2, r_3$ , and  $r_4$ , where the distance between two consecutive positions is 5 cm. The magnetic field is measured backwards and forwards.

$$j = \frac{I}{2\pi zr} \quad (62)$$

The total current can be related to the resistance via Ohm's law:

$$\Delta V = R(r)I(r) \quad (63)$$

where  $\Delta V$  is the potential difference between the middle electrode and the outer electrodes. Substituting  $I$  in the expression of current density, we have:

$$j = \frac{\Delta V/R(r)}{2\pi zr} \quad (64)$$

## F. Induced Magnetic Field

In this section, we derive the expression of induced magnetic field in the flow due to the rotation of the fluid. The external axial magnetic field and the radial electric field give rise to Lorentz force  $\mathbf{j} \times \mathbf{B}$  which is applied to the electrons and as well as the ions. In the fluid, the number of electrons is equal to the number of ions. The velocity of the electrons is almost equal to the velocity of ions. Therefore the potential difference generated is very small leading to a negligible electric field.

Ampere's Law states that:

$$\oint \mathbf{B} \cdot d\mathbf{l} = \mu_0 I \quad (65)$$

where  $d\mathbf{l}$  is an infinitesimal element (a differential) of an amperian loop,  $\mu_0$  is the permeability of free space, and  $I$  is the total current enclosed in this loop. Ohm's Law states that the current in a closed loop generates an induced magnetic field, which we will call  $B_{ind}$ . Since the electric field is negligible, the current is negligible and thus the induced magnetic field is very small.

Using a teslameter equipped with two types of probes, we measured the magnetic field. One of the probes has a flattened tip to measure the magnetic field parallel to the probe. Another probe has a cylindrical shape to measure the magnetic field perpendicular to the probe. In both cases, the induced magnetic field was found to be null. We also measured low magnetic field corresponding to the magnetic field fluctuations. No fluctuations appeared to exist. This is an important experimental measurement, verified

by theory. Magnetic fluctuations are a necessary ingredient in magnetorotational instability as defined by Balbus [15]. This shows that the instability of this experiment is purely hydrodynamical.

### G. Laser Diagnostics

The aim of the experiment is to obtain information about the dynamics of the flow by measuring properties of the fluid velocity. As we have stated before, the Lorentz force is proportional to the magnitude of electric current. As the Lorentz force increases, the fluid angular rotation  $\Omega$  increases.

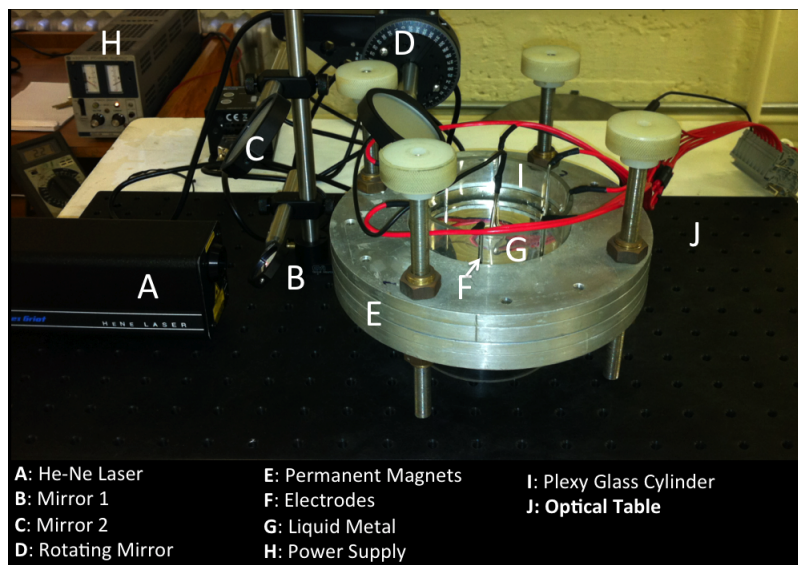


Figure 29: Experimental setup for data collection. A: He-Ne Laser B: Mirror 1 C: Mirror 2 D: Rotating Mirror E: Permanent Magnets F: Electrodes G: Liquid Metal H: Power Supply I: Plexy Glass Cylinder J: Optical Table.

Galinstan has a reflective surface. Laser reflection and optical equipment are used in the experiment in compliance with the reflective feature of the fluid. A set of three

mirrors are used to direct a He-Ne laser beam of diameter 0.47 mm and a wavelength of 633 nm to the reflective surface of the fluid. The first two mirrors are kept fixed, while the third mirror is attached to an automated rotator. The automated mirror is managed through PRM1Z8, which is a precision motorized rotation mount. Rotation is driven via a DC001 DC servo controller equipped with high ratio gearbox (67:1). This controller is a companion of PRM1Z8 for achieving smooth continuous motion. The rotation of the mirror is managed either through the software interface APTuser or by using a Vernier dial. The precision DC motor actuator provides 1 arcsecond resolution over the 360° rotation. Each angular rotation of the rotator mirror corresponds to a radial translation of the laser spot on the surface of the fluid. Laser reflections on the ceiling are captured by USB CMOS Color Camera at a chosen rate (for example, 35 frames/second). Videos of the laser spot position on the screen are collected to be analyzed. The data processing method and the experimental results are presented in the next chapter.

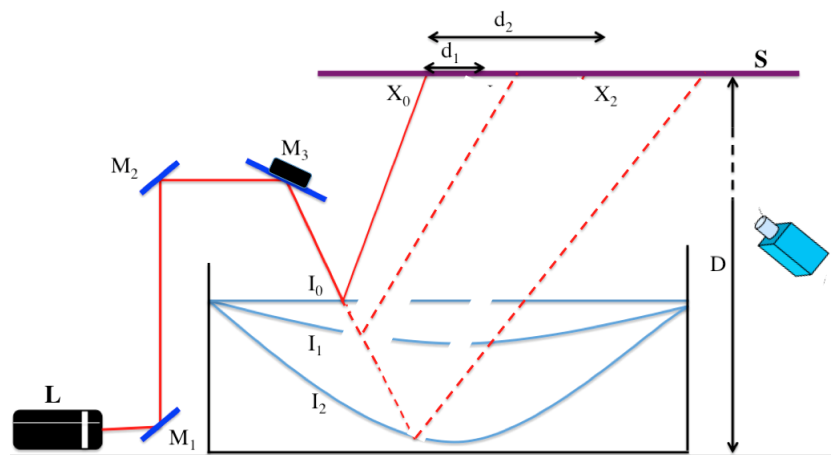


Figure 30: Schematic drawing showing the idea behind the experimental method.

## H. Fluid Distortions

Rotation of the fluid causes a variation in the height of the fluid. In this section, we find the relation between the distances between laser reflections that are captured on camera and angles of distortion. When the fluid is at rest, a laser beam shining on the surface is reflected to a screen at point  $P$ . A distortion of the surface in the parallel direction moves  $P(x_0, y_0)$  to  $S(y_{\parallel}, x_{\parallel})$ . The angle between the fluid surface and the plane parallel to the plane of the laser beam is denoted by  $\alpha_{\parallel}$ . A distortion of the surface in the perpendicular direction moves  $P$  to  $Q(x_{\perp}, y_{\perp})$ . The angle between the fluid surface and the plane perpendicular to the plane of the laser beam is denoted by  $\alpha_{\perp}$ . One can easily see that  $y_0 = y_{\parallel}$  and  $x_{\perp} = x_{\parallel}$ . By simple geometric interpretation, we can determine  $\alpha_{\perp}$  by measuring  $x_{\parallel}$  on the screen:

$$\tan\alpha_{\parallel} = \frac{x_{\parallel}}{D} \quad (66)$$

If the laser beam is directed on the fluid at a distance  $\delta$ , and the fluid height is  $h$ , one can see that:

$$\tan\alpha_{\parallel} = \frac{x_{\parallel}}{D} = \frac{\delta}{D} \frac{\partial h}{\partial r}$$

## I. Shallow Water Equations

The Shallow Water Equations (SWE) form a 3-by-3 system of variables  $(u_r, u_{\theta}, h)$ . We will show that this set of equations can be used in order to determine the velocity in the  $\theta$ -direction of a rotating reflective fluid by simply measuring the variations of  $h$ .

$$\frac{\partial u_r}{\partial t} - f u_{\theta} = -g \frac{\partial h}{\partial r} \quad (67)$$

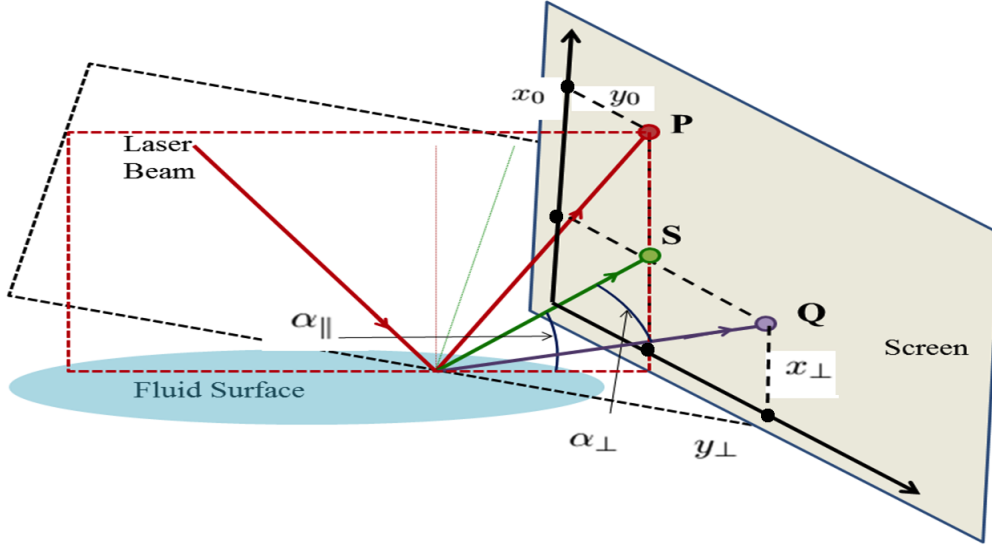


Figure 31: An incident beam of the laser falling on the surface is reflected by the fluid to point  $P$  on the screen. When a passing wave deflects the surface by an angle  $\alpha_{\perp}$ , the beam is reflected to point  $S$  on the screen. When a passing wave deflects the surface by an angle  $\alpha_{\parallel}$ , the beam is reflected to point  $Q$  on the screen.

$$\frac{\partial u_{\theta}}{\partial t} + f u_r = -\frac{g}{r} \frac{\partial h}{\partial \theta} \quad (68)$$

$$\frac{\partial h}{\partial t} = -z \left( \frac{\partial u_r}{\partial r} + \frac{1}{r} \frac{\partial u_{\theta}}{\partial \theta} \right) \quad (69)$$

where  $f$  is the Coriolis coefficient associated with the Coriolis force, on Earth equal to  $2\Omega \sin(\phi)$ , where  $\Omega$  is the angular rotation and  $\phi$  is the latitude.

For the steady state solution and for  $\phi = \pi/2$ ,  $f = 2\Omega = 2u_{\theta}/r$ :

$$u_{\theta}^2 = \frac{gr}{2} \frac{\partial h}{\partial r} \quad (70)$$

The above equation relates the velocity in the  $\theta$ -direction to  $\partial h/\partial r$ .

By shining a laser beam at the surface of the fluid at a distance  $\delta$  from the



center, we obtain a laser reflection on the screen. The planar variations of the position of the laser reflection point on the screen are denoted by  $x_{total}$  and  $y_{total}$ . Since the surface of the fluid can move by two angles,  $\alpha_{\perp}$  and  $\alpha_{\parallel}$  as shown in Fig.(33) and (34), we associate with these angles two position variations;  $y_{\parallel}$  and  $y_{\perp}$ , where  $y_{total} = y_{\perp} + y_{\parallel}$ . However, the variation in the  $x$ -axis is unidirectional such that  $x_{\perp} = x_{\parallel}$ . By geometric interpretation, it was found that  $x_{\parallel}/D = \tan(\alpha_{\parallel})$ . Therefore, by capturing the variations of the laser spot on video and performing data processing procedure,  $x_{\parallel}$  can be determine. As a result of finding  $x_{\parallel}$ ,  $\alpha_{\parallel}$  can be obtained by calculation. Then we relate  $\alpha_{\parallel}$  to the variation of the height in the  $r$ -direction. This variation is linked to  $\alpha_{\parallel}$  via  $\tan\alpha_{\parallel} = (\delta/D)\partial h/\partial r$ . Through shallow water equations we relate the variations in height to the velocity component in the  $\theta$ -direction,  $u_{\theta}^2 = gr/2(\partial h/\partial r)$ . Fig.(32) summarizes these ideas.

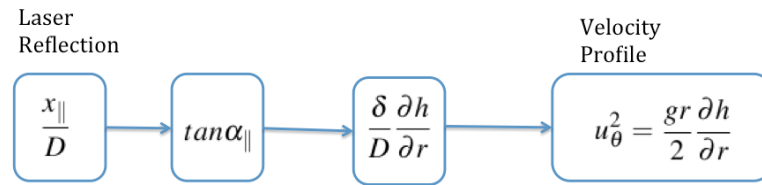


Figure 32: Experimental method to find the azimuthal velocity.

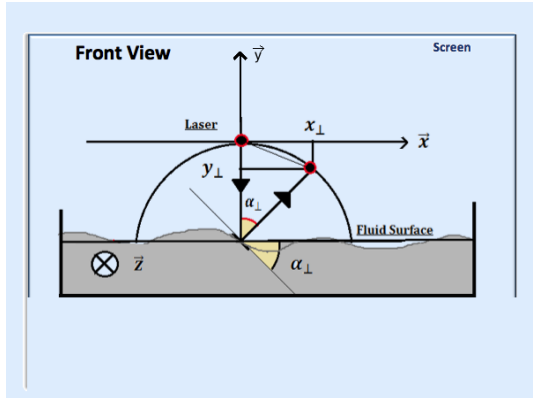


Figure 33: Laser shining on the surface of the fluid showing the surface deflection perpendicular to the plane of the laser beam.

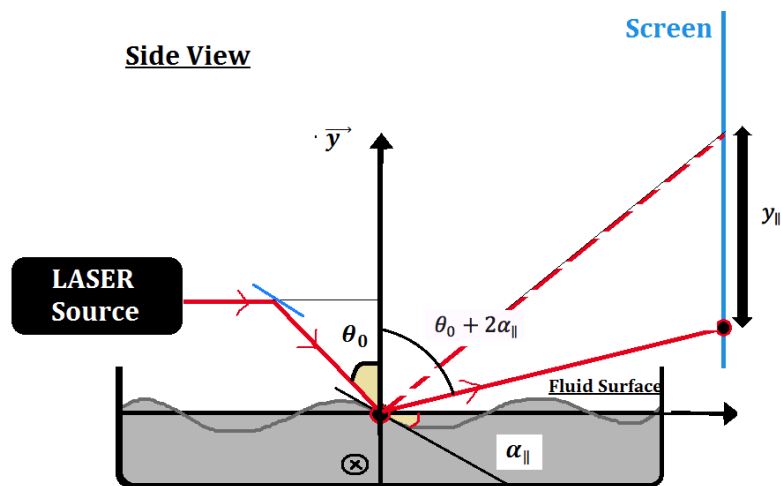


Figure 34: Laser shining on the surface of the fluid showing the surface deflection parallel to the plane of the laser beam.

## J. Dimensionless Numbers

Dimensionless parameters are calculated in order to compare experimental results. Reynolds number is found to be  $10^4$ . This signifies that the inertial forces are much higher than the viscous force. Hartmann number is equal to  $10^5 + 163$ . This implies that the electromagnetic forces dominate over the viscous force. Prandtl number is found to be  $10^6$  which means that conduction in the flow is much larger than convection of heat. The Hartman layer as found to be  $10^{-4}$  which is less than 2% of the radius of the container. The Ekman number was found to be  $10^{-5}$  which is less than 0.2% of the radius of the container. The dimensionless parameters of the TRF are given in Table (4).

Table 4: Dimensionless Numbers TRF

Critical Number	Symbol	Expression	Value
Reynolds Number	Re	$VR/\nu$	$10^4$
Prandtl Number	Pr	$\nu/\kappa$	$10^6$
Hartman Number	Ha	$\sqrt{\sigma \Delta VB/\mu u} + \sqrt{\sigma B^2 L^2/u}$	$10^5 + 163$
Hartman Layer [m]	HaL	$\mu/\sqrt{\sigma B^2}$	$10^{-4}$
Ekman Number	$E_k$	$\nu/(\Omega R^2)$	$10^{-5}$
Ekman Layer[m]	$\delta$	$\sqrt{\nu/\Omega}$	$10^{-4}$

## K. Conclusion

- The experimental apparatus and its setup dimensions are introduced. The characteristics of the fluid used as well as its physical properties are explained and compared to water.
- The external magnetic field dependence on  $r$ . was found to be  $B(r) = -7r^2 + 70r - 258$ .
- The current density dependency on  $r$  is determined.
- The rotation of the conducting fluid results in an induced current density. The induced magnetic field is found to be negligible.
- An experimental diagnostic tool using a laser and a set of mirrors is developed. The method relates the laser reflections to the variations of the height of the fluid as it becomes distorted.
- The velocity in the  $\theta$ -direction is related to the height via a set of equations called Shallow Water Equations.
- Dimensionless parameters of the fluid are also specified.

CHAPTER V  
EXPERIMENTAL RESULTS

## A. Introduction

Two types of experiments are conducted to understand the dynamics of a thin rotating flow. The experiments distinguish between two types of motion. The first type is a large scale motion due to the rotation of the fluid as shown in Fig.(35). The second type is a small scale motion caused by an instability of the flow.

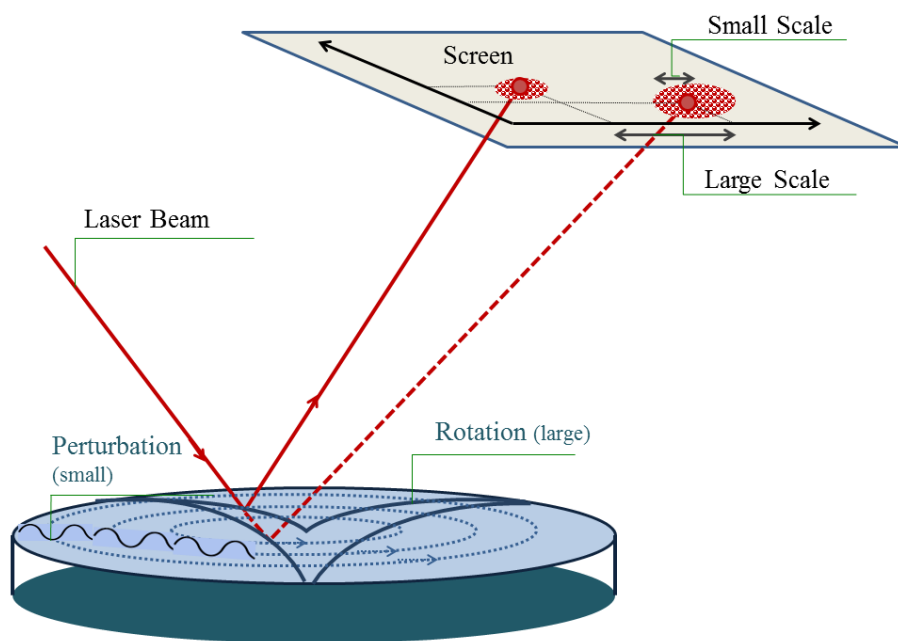


Figure 35: Distortion of the fluid surface caused by the rotation of the flow leads to large scale motion. Perturbation of the distorted surface due to instabilities leads to small scale motion.

In the first experiment, we focus on probing the fluid surface at fixed positions as function of current. Analysis of the collected data allows us to determine the unstable region of the flow. We also determine the onset of instability as function of electric current. In the second experiment, we aim at understanding the dynamics of the flow by probing

the fluid surface along the radius for a fixed electric current. Using this experiment, we determine the onset of instability as function of radial position. In this chapter, we describe the method of data collection, the analysis procedure and the experimental results and plots.

### B. Experiment I: Motion as function of Electric Current

In order to study the dynamics at different positions as a function of the current, the laser spot on the flow is set and the current is increased. Four different positions are chosen, they are at 0.7, 2, 3 and 4 cm away from the central electrode. As pointed out earlier, the fluctuations appear to be important for distances close to the central electrode. For each position and current, a movie of the reflected beam from the flow surface is recorded. The number of frames per movie is 2000 recorded at a resolution of 1024x768 pixels and at a rate of 30 frames/second. Each frame is then analyzed by a Matlab code written to detect accurately the maximum of the laser intensity on the screen.

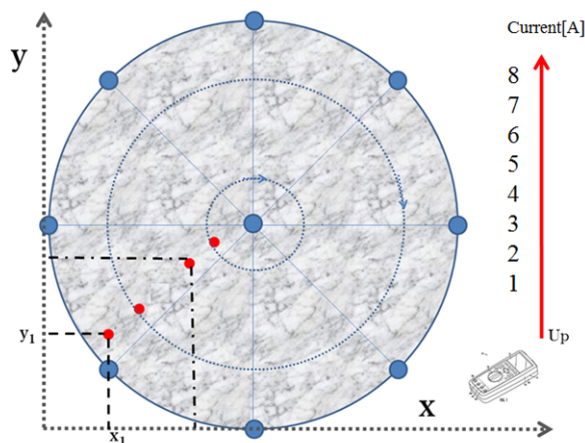


Figure 36: In the first experiment, measurements at four different positions of the fluid surface are collected. At each position, measurements of eleven values of the current are taken.

A plot of light intensity in each frame indicates the location in pixels of the laser spot. The highest intensity of light in each image is the indicator of the center of the laser reflection. In a plot of intensity of light, the black screen is shown to be blue corresponding to lowest intensity and the red laser spot is shown to be brown corresponding to the highest intensity. Between the two extremes lies a spectra of gradual increase from lowest to highest intensity of light. The laser spot reflection has highest intensity at the middle of the spot. To further increase the fine variations of the intensity of light, a filter is applied to each frame. The resulting image is shown Fig.(37).

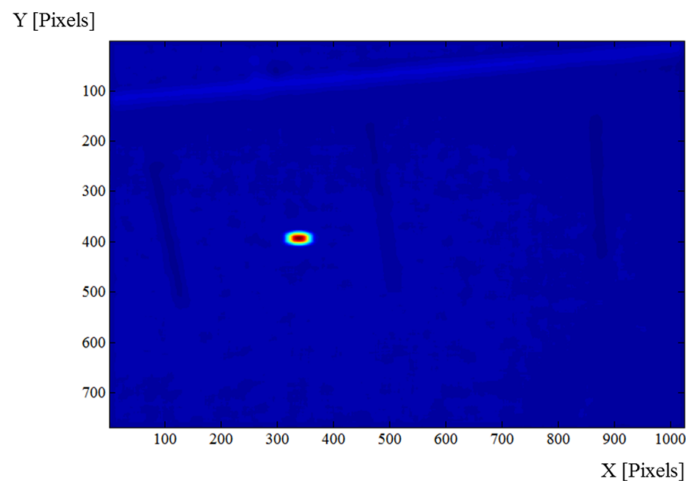


Figure 37: The laser reflection on the screen is analyzed by MATLAB as the point of highest intensity. A filter is applied to sharpen the image.

The position is denoted by  $(X_{max}, Y_{max})$ . Now, by following the behavior of the laser position as a function of time, one can deduce whether a turbulent regime has taken place. For laminar flows, the position of the laser beam does not deviate from its position;



When turbulence occurs, the laser spot on the screen vibrates and its position variation reflects the onset of eddies which are rotating with the mean flow. Fig.(38) shows the position of the laser spot on the screen, represented by  $X_{max}$  and  $Y_{max}$  in arbitrary units for increasing total current in the flow. The laser is at 2 cm from the inner electrodes. At low values of the current,  $I = 3$  A, the 2000 points, reflecting the position the laser for 2000 frames are packed together. The deviation from the average position is small of the order of the modifications when no current is applied to the flow. As the current is increased from 3 to 4 A, the deviation from the average position has increased but not enough to indicate the presence of turbulence. The cloud representing the laser spot position as a function of time, dramatically increase in the area occupied for a current of 5 A. This tendency continues when increasing the current even more reaching 8 A. At this level, the deviation from the average position is now important, clearly reflecting the onset of turbulent fluctuations. From this figure, one can safely deduce that the flow becomes turbulent with increasing current at positions close to the inner electrode.

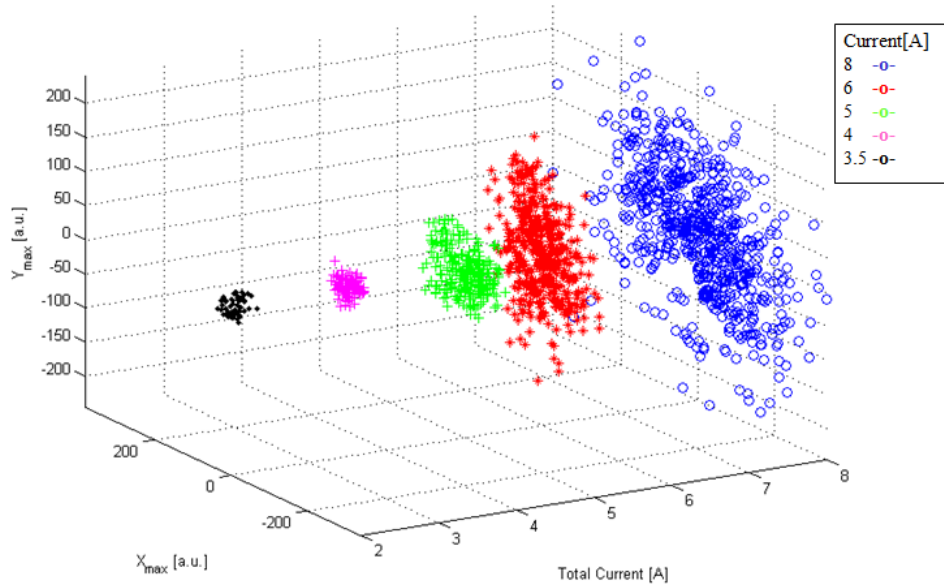


Figure 38: Plot of laser reflections as function of current showing an increase of the distances between them as an indication of growing instability.

We turn now into quantifying this deviation from the average position as a function of current and for different positions of the laser on the flow surface. For this purpose, we determine the average position and subtract each position from the average one in a way that we have the fluctuating part around 0. Next, the standard deviation of the distance to the center is determined. The values of  $\sigma$  are plotted as a function of  $I$  for different positions in Fig.(39). For positions of the laser at 4 cm from the inner electrode, the standard deviation remains almost unchanged with increasing current. It remains close to 5 independently of the current value. One can safely deduce that this part of the fluid remains laminar even at a total current of 8 A. At 3 cm, represented by the crosses, the value of  $\sigma$  remains unchanged up to  $I = 7$  A where a small increase is detected and it will deviate even more for  $I = 8$  A. For the position of the laser even closer, at  $r = 2$  cm, the standard deviation increases at low currents, around 2-3 A but one can show that this

increase is partly caused by that of the laser spot size on the screen. For  $I > 6$  A, we detect a systematic increase. One is thus tempted to deduce that the flow closer to the inner electrode are unstable whereas far the perturbation is still small. Consequently, a strong radial gradient exists in this flow. This is made even clearer when the laser spot is brought to 1.5 cm from the inner electrode. The standard deviation increases similarly as at  $r = 2.5$  cm for low currents but a clear difference is reported for  $I > 5$  A where the standard deviation increases with the current. One may thus deduce from Fig.(39) two conclusions. It appears that the onset of turbulence takes place close to the electrode and that there exist a strong radial gradient which reflects a decrease of the fluctuations with increasing distance to the inner electrode.

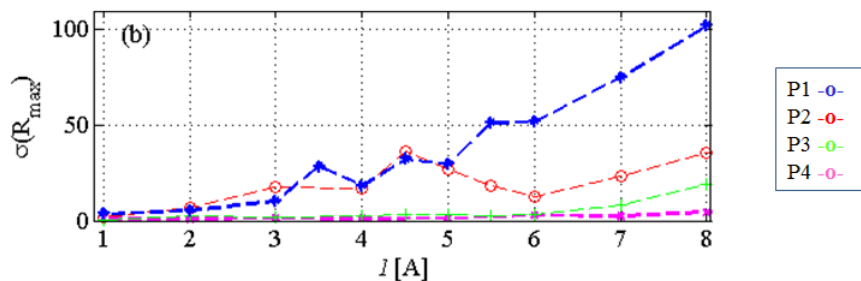


Figure 39: Plot of standard deviations versus current at four different positions of the fluid.

### C. Experiment II: Motion as function of Radial Position

In the previous experiment, we could deduce that the region near the inner electrode is unstable. To obtain a more precise interpretation, the current is fixed and the radius is varied. In  $(x,y)$  coordinates, the starting point of the measurement is a point

$A(x_0, y_{start})$  near the outer electrode. The laser beam is directed via the rotator mirror to probe the surface in a straight line until it reaches a point  $B(x_0, y_{end})$  as shown in Fig.(40). The laser beam is reflected by the surface to reach the screen situated parallel to the fluid surface.

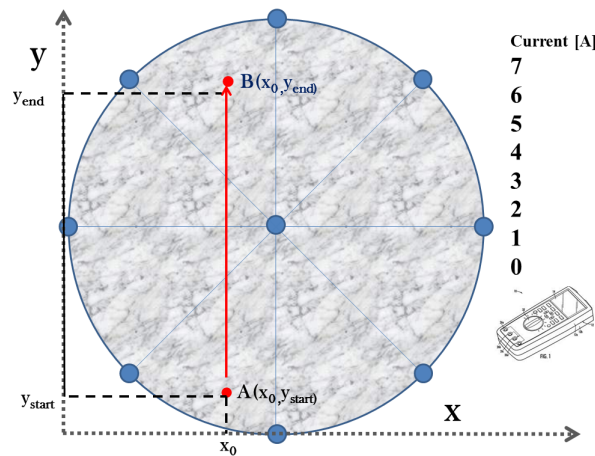


Figure 40: In the second experiment, the laser beam probes the surface of the fluid. This measurement is collected for eight different values of the current.

### 1. Steady State

The radius is probed from one outer electrode to another in a video of 100 frames. For eight values of the current, videos of the laser reflection are recorded and analyzed. In each frame, the position of the laser reflection is determined. It is denoted by  $(X_{max}, Y_{max})$ . An overlay of the maxima produces a trajectory of the laser reflection. By following the change in trajectory as function of current as shown in Fig.(41), one can understand the motion taking place on the fluid surface. For low currents, the trajectory follows a hill near the central electrode. For  $I = 3$  A and above, the trajectory continues to increase but

instead of decreasing back, the trajectory rotates in an oval shape. This takes place near the central electrode. And the oval enlarges with increasing current.

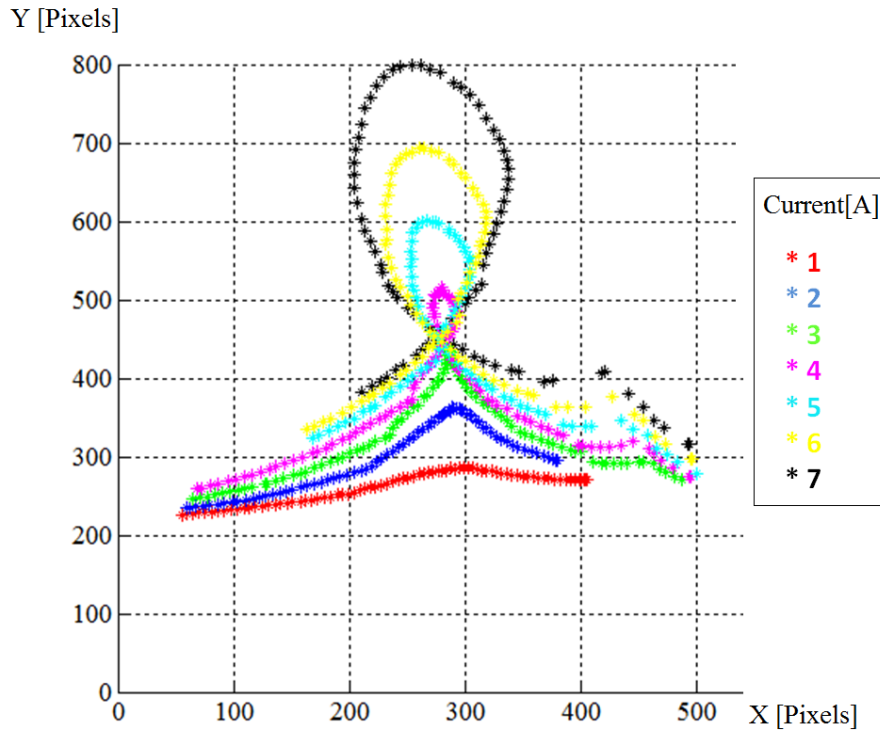


Figure 41: Trajectory of laser reflection for several currents between 1 and 7 A.

Furthermore, we notice that there is an offset between the starting points of the trajectories. This happens even though the rotator mirror returns the laser light back to the same point on the fluid for all currents.

The fluid rotates around the central electrode due to Lorentz force. This rotation deflects the surface such that the fluid near the outer electrode is at a higher level than the fluid near the inner electrode. As the force increases, the surface of the fluid becomes more sharply deflected. The angle of deflection can be projected is due to  $\alpha_{\parallel}$  and  $\alpha_{\perp}$ .

This leads to large scale motion of the laser reflection on the screen.

Also the distortion is caused by perturbations due to instabilities in the flow. We can imagine the perturbation as a wave passing on the surface of the fluid. This wave also distorts the already deflected fluid surface. Thus, it also changes the position of the laser reflection on the screen. However, the magnitude of the perturbation is small, giving rise to small scale motion of the laser.

We can conclude from Fig.(41) that the angles of deflection  $\alpha_{\perp}$  and  $\alpha_{\parallel}$  increase with increasing current. Furthermore, the trajectory followed by the laser beam is due to two types of motion that are inseparable at this stage. In order to distinguish between the two types of motion, we probe the motion along the radius versus time in the next experiment.

## ***2. Unsteady State***

In the previous section, the dynamics were studied versus radius. In this section, we study the dynamics versus time. For this purpose, a measurement of the laser reflection versus radius was repeated five times. Three videos of 600 frames each were recorded such that the radius is probed from  $A$  to  $B$  and two videos were recorded such that the laser beam moves from  $B$  to  $A$ . This is done to ensure that there is no variation in the choice of motion. Although the videos start from a specific radial point, it is not guaranteed that the first frame captures this point. Therefore, the offset in frames was taken into consideration during the image processing using Matlab. After determining the maximum point in each frame of the five trajectories corresponding to five measurements an average trajectory is calculated. Error bars of the average were also found. Fig.(42) is a plot of the average along with its error bars. It is worth mentioning that the two strong deviations between 270 and 280 and between 315 and 320 are experimental errors. It was confirmed by reviewing

the video that these deviations are not related to the actual dynamics of the fluid.

Each point of the curve shown in Fig.(42) is the summation of horizontal and vertical displacement of the laser spot on the plane of the screen. If we plot the vertical component only of each of the five measurements as well as the vertical component of the average, we obtain the upper curve in Fig.(43). The measurements perfectly fit with slight variation from the average. The curve shows that the value of  $y$  increases to reach a maximum of at 180 pixels and then decreases back to almost the same value. This increase makes the trajectory turn as function of  $x$ . The position of the maximum is the center of the cylindrical container which will appear to be important for the next analysis. At this stage, the onset of instability is not clear.

Next, the standard deviation of the  $y$ -component is plotted versus position in pixels for the 600 frames of the 5 videos. Here, we start to see a pattern. As we have indicated from the upper plot of Fig.( 31), the center is at around 180 pixels. The standard deviation is found to be high between 180 and 280 pixels, and then it encounters a sharp decrease until 360 pixels. One can safely conclude that the region near the central electrode is higher standard deviation. This is an indication of the instability. This allows us to determine the unstable region. However, the region is obtained in terms of pixels. Since a video is recorded, the radial position of the laser beam can help us determine the onset in centimeters.

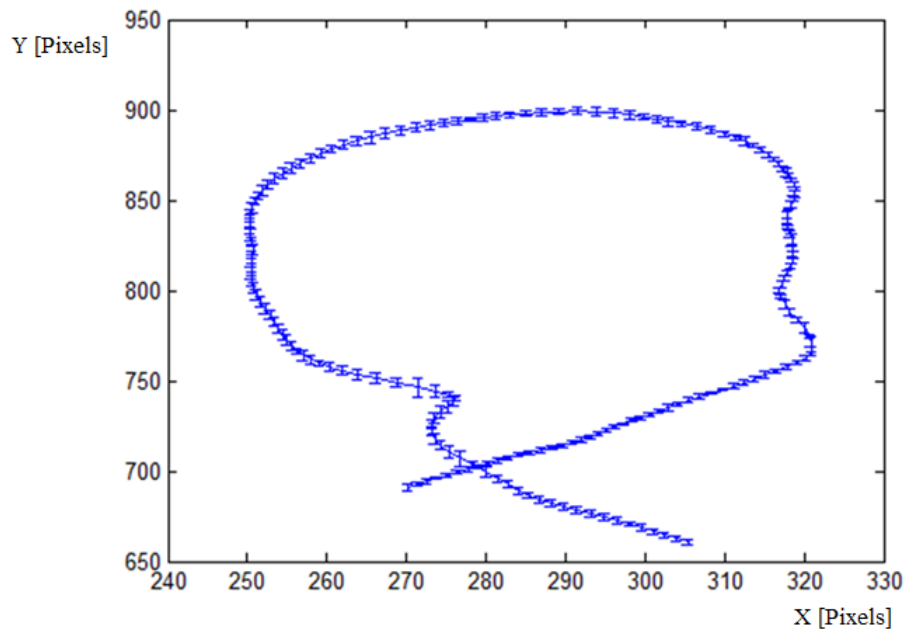


Figure 42: An average trajectory along with error bars of the same measurement of probing the surface at fixed current repeated 5 times.

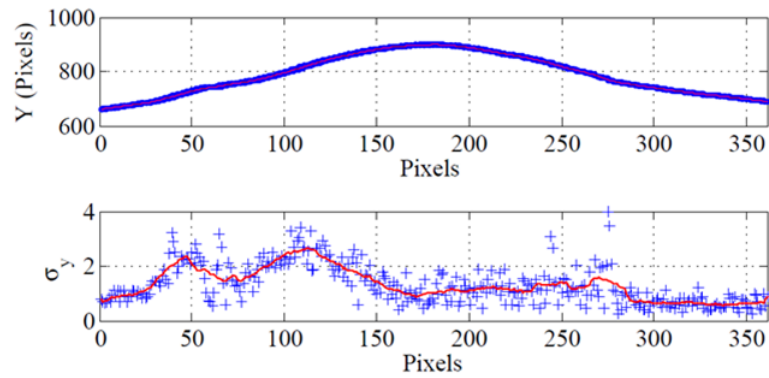


Figure 43: Up: The average  $Y$  component (red line) along with the  $Y$  components of the five measurements (blue). Down: Standard deviation of the  $Y$  component (blue) and smoothing of the curve (red).

As the above data has given us an idea of the region of instability. We proceed



further by trying to find a relation between the position in pixels in the image and the actual radial position of the onset of instability. While probing the fluid surface, a certain distance  $d_{fluid}$  is covered. Also the distance which encloses the trajectory followed by the laser reflection can be obtained from the image. Let us denote it by  $d_{pixels}$ . The ratio  $d_{fluid}/d_{pixels}$  allows us to construct a vector that transforms the image from pixels to centimeters. Plotting the standard deviation versus this vector is the curve obtained in Fig.(44). It is the variation of the  $y$ -component versus radius in cm. The standard deviation for  $0 < r < 1.5$  is around 1.4. At  $r = 1.5$ , the standard deviation is reduced by half and continues to be around 0.6 until 3 cm. This is a strong indication of the onset of the instability at  $r = 1.5$  cm.

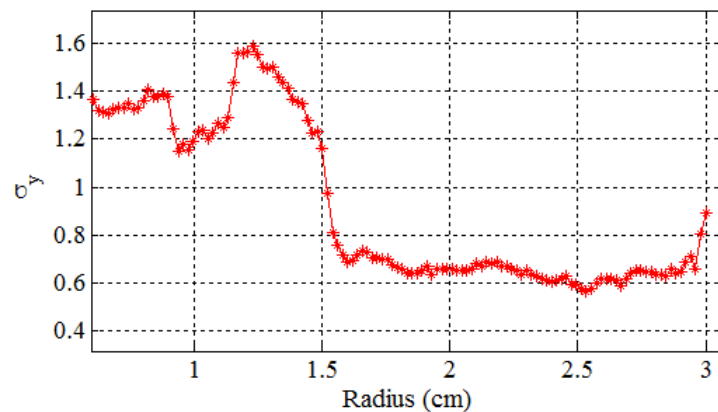


Figure 44: Plot of the standard deviation of the  $y$ -component of the position of the laser reflection versus radius.

#### D. Conclusion

Two types of experiments were conducted. The first experiment studies the dynamics of the flow as function of current. Analysis of the captured videos determines the

coordinates of the point of maximum intensity in each frame of the video. An overlay of the position  $(X_{max}, Y_{max})$  of all maxima allows us to visualize the distances between the point. The plot of maxima versus current shows that the distances between maxima increases with increasing current. These distances are a measure of the velocity fluctuations of the flow. Furthermore, the standard deviation of each individual maxima from the average is determined and plotted versus current. For the positions away from the center, the standard deviation was found to be small. However, for the position closest to the middle electrode, the standard deviation shows a sudden increase at  $I = 6$  A giving an evidence of the onset of the instability.

The second type of experiment investigates the dynamics of the fluid as function of radius. In the first part, measurements were recorded for several values of the current. The trajectory of the laser beam was reported. Two types of motion were discussed. In the second part, the motion is studied versus time. A plot of the standard deviation for 5 measurements allowed us to deduce that the region near the middle electrode is stable. Furthermore, a plot of standard deviation versus radius allows us to accurately determine the onset of the instability as function of radius.

# CHAPTER VI

## CONCLUSION

## A. Personal Achievements

- Determined the base flow of the Thin Rotating Flow and compared the result to the base flow of Taylor-Couette Flow.
- Applied stability analysis by introducing a perturbation term to the azimuthal component of the velocity.
- Analyzed the resulting dispersion relation and obtained a stability condition for the flow.
- Built an experimental setup using a liquid metal, Galinstan, to test the theoretical predictions.
- Developed the laser diagnostic technique and executed the experiment.
- Analyzed the result and determined the onset of instability versus current and radial position.

## B. Future Work

The theoretical development of this thesis expanded during the course of understanding the properties of the flow. The experimental work gained more perspective with a theoretical foundation. When we turned to explore the theory, we learned that hydrodynamic instabilities are extensively studied in the  $(r, z)$ -plane of cylindrical setups. In order to derive the conditions of stability  $(r, \theta)$ -plane, we performed a stability analysis with an assumption that the height of the fluid is very small and that the perturbation of the velocity takes place in the  $\theta$ -direction.

In the future, the stability analysis can be performed in the cylindrical geometry. Certain mathematical challenges will arise, but approximations can be applied. Further-

more, the assumptions of the perturbation method can be reduced.

Some simulations were done for this experiment. This has inspired us with ways to advance the experiment. By simulation methods, it was found that the velocity profile of continuous conductors at the boundary of the setup is close to the eight-electrode configuration. However, it would be interesting to experimentally examine the difference. A thin sheet of metal can be assembled into a cylinder with exact dimensions of the plexy-glass container. It can replace the eight electrodes.

Although the fluid used in this thesis has distinctive properties, another conductive fluid can be used. However, the laser diagnostics method only applies for reflective surfaces. Furthermore, the height of the plexiglass container can be reduced for better laser diagnostics. The distance between the fluid surface and the screen was dictated by the height of the laboratory room. This presented a challenge for experimental measurements. Other possible geometric configurations of the experiment could be investigated.

## BIBLIOGRAPHY

- [1] Ronald C Kessler, Sandro Galea, Russell T Jones, and Holly A Parker. Mental illness and suicidality after hurricane katrina. *Bulletin of the World Health Organization*, 84(12):930–939, 2006.
- [2] Patrick J McCarthy. Elie, manitoba, canada, june 22, 2007: Canada’s first f5 tornado. In *24th Conference on Severe Local Storms*, 2008.
- [3] Peter RN Childs. *Rotating flow*. Access Online via Elsevier, 2010.
- [4] A Mallock. Experiments on fluid viscosity. *Philosophical Transactions of the Royal Society of London. Series A, Containing Papers of a Mathematical or Physical Character*, 187:41–56, 1896.
- [5] Maurice Frédéric Alfred Couette. *Etudes sur le frottement des liquides*. PhD thesis, 1890.
- [6] Lord Rayleigh. On the dynamics of revolving fluids. *Proceedings of the Royal Society of London. Series A*, 93(648):148–154, 1917.
- [7] Russell J Donnelly. Taylor-couette flow: the early days. *Phys. Today*, 44(11):32–39, 1991.
- [8] Donald Coles. Transition in circular couette flow. *Journal of Fluid Mechanics*, 21(03):385–425, 1965.

- [9] HA Snyder. Stability of rotating couette flow. i. asymmetric waveforms. *Physics of Fluids*, 11:728, 1968.
- [10] ER Krueger, A Gross, and RC Di Prima. On the relative importance of taylor-vortex and non-axisymmetric modes in flow between rotating cylinders. *J. Fluid Mech*, 24(3):521–538, 1966.
- [11] Lee Paul Graves, James C. McWilliams, and Michael T. Montgomery. Vortex evolution due to straining: a mechanism for dominance of strong, interior anticyclones. *Geophysical Astrophysical Fluid Dynamics*, 100(3):151–183, 2006.
- [12] HA Snyder. Waveforms in rotating couette flow. *International Journal of Non-Linear Mechanics*, 5(4):659–685, 1970.
- [13] C David Andereck, R Dickman, and Harry L Swinney. New flows in a circular couette system with co-rotating cylinders. *Physics of Fluids*, 26:1395, 1983.
- [14] MJ Burin, H Ji, E Schartman, R Cutler, P Heitzenroeder, W Liu, L Morris, and S Raftopolous. Reduction of ekman circulation within taylor-couette flow. *Experiments in fluids*, 40(6):962–966, 2006.
- [15] Steven A Balbus. Magnetorotational instability. *Scholarpedia*, 4(7):2409, 2009.
- [16] Steven A Balbus and John F Hawley. A powerful local shear instability in weakly magnetized disks. i-linear analysis. ii-nonlinear evolution. *The Astrophysical Journal*, 376:214–233, 1991.
- [17] Akira Kageyama, Hantao Ji, Jeremy Goodman, Fei Chen, and Ethan Shoshan. Numerical and experimental investigation of circulation in short cylinders. *arXiv preprint physics/0405123*, 2004.

- [18] Jeremy Goodman and Hantao Ji. Magnetorotational instability of dissipative couette flow. *Journal of Fluid Mechanics*, 462:365–382, 2002.
- [19] Wei Liu, Jeremy Goodman, Isom Herron, and Hantao Ji. Helical magnetorotational instability in magnetized taylor-couette flow. *Physical Review E*, 74(5):056302, 2006.
- [20] G Rudiger and R Hollerbach. Comment on“helical magnetorotational instability in magnetized taylor-couette flow”. *PHYSICAL REVIEW-SERIES E-*, 76(6):068301, 2007.
- [21] J Sommeria. Experimental study of the two-dimensional inverse energy cascade in a square box. *Journal of fluid mechanics*, 170:139–168, 1986.
- [22] VM Canuto, A Howard, Y Cheng, and MS Dubovikov. Ocean turbulence. part i: One-point closure model-momentum and heat vertical diffusivities. *Journal of Physical Oceanography*, 31(6):1413–1426, 2001.
- [23] P Tabeling, S Burkhart, O Cardoso, and H Willaime. Experimental study of freely decaying two-dimensional turbulence. *Physical review letters*, 67(27):3772–3775, 1991.
- [24] Sergey Danilov, FV Dolzhanskii, VA Dovzhenko, and VA Krymov. Experiments on free decay of quasi-two-dimensional turbulent flows. *Physical Review E*, 65(3):036316, 2002.
- [25] HJH Clercx, GJF Van Heijst, and ML Zoetewij. Quasi-two-dimensional turbulence in shallow fluid layers: the role of bottom friction and fluid layer depth. *Physical review E*, 67(6):066303, 2003.



- [26] LM Moubarak and GY Antar. Dynamics of a two-dimensional flow subject to steady electromagnetic forces. *Experiments in fluids*, 53(5):1627–1636, 2012.
- [27] GJF Van Heijst, HJH Clercx, and D Molenaar. The effects of solid boundaries on confined two-dimensional turbulence. *Journal of Fluid Mechanics*, 554:411–432, 2006.
- [28] Patrick Tabeling. Two-dimensional turbulence: a physicist approach. *Physics Reports*, 362(1):1–62, 2002.
- [29] HJH Clercx and GJF van Heijst. Two-dimensional navier-stokes turbulence in bounded domains. 2009.
- [30] Louis N Howard and AS Gupta. On the hydrodynamic and hydromagnetic stability of swirling flows. *Journal of Fluid Mechanics*, 14(03):463–476, 1962.
- [31] S Chandrasekhar. The stability of non-dissipative couette flow in hydromagnetics. *Proceedings of the National Academy of Sciences of the United States of America*, 46(2):253, 1960.
- [32] Hantao Ji, Jeremy Goodman, and Akira Kageyama. Magnetorotational instability in a rotating liquid metal annulus. *Monthly Notices of the Royal Astronomical Society*, 325(2):L1–L5, 2001.
- [33] Steven A Balbus and John F Hawley. Instability, turbulence, and enhanced transport in accretion disks. *Reviews of modern physics*, 70(1):1, 1998.
- [34] Wei Liu, Jeremy Goodman, Isom Herron, and Hantao Ji. Helical magnetorotational instability in magnetized taylor-couette flow. *Physical Review E*, 74(5):056302, 2006.

- [35] Hantao Ji, Jeremy Goodman, Akira Kageyama, Michael Burin, Ethan Schartman, and Wei Liu. Magnetorotational instability in a short couette flow of liquid gallium. In *AIP Conference Proceedings*, volume 733, page 21, 2004.
- [36] K Noguchi, VI Pariev, SA Colgate, HF Beckley, and J Nordhaus. Magnetorotational instability in liquid metal couette flow. *The Astrophysical Journal*, 575(2):1151, 2002.
- [37] NB Morley, J Burris, LC Cadwallader, and MD Nornberg. Gainsn usage in the research laboratory. *Review of Scientific Instruments*, 79(5):056107–056107, 2008.

